Title:

A neonatal mouse model characterizes transmissibility of SARS-CoV-2 variants and reveals a role for ORF8

Authors:

Bruno A. Rodriguez-Rodriguez[1], Grace Ciabattoni[1], Ana M. Valero-Jimenez[1], Keaton M. Crosse[1], Austin Schinlever[1], Joaquin Rodriguez Galvan[1], Ralf Duerr[1], Marisa McGrath[2], Ludovic Desvignes[3,4], Matthew Frieman[2], Mila B. Ortigoza[1]*, and Meike Dittmann[1]*

Affiliations:

[1]Department of Microbiology, New York University Grossman School of Medicine, New York, New York, USA

[2]Department of Microbiology and Immunology, University of Maryland School of Medicine, Baltimore, MD 21201

[3]Department of Medicine/Division of Infectious Diseases and Immunology, New York University Grossman School of Medicine, New York, New York, USA

[4]High Containment Laboratories - Office of Science and Research, NYU Langone Health, New York, New York, USA

*Co-corresponding authors

Abstract

Small animal models have been a challenge for the study of SARS-CoV-2 transmission, with most investigators using golden hamsters or ferrets. Mice have the advantages of low cost, wide availability, less regulatory and husbandry challenges, and a versatile reagent and genetic toolbox. However, adult mice do not transmit SARS-CoV-2. Here we establish a model based on neonatal mice that allows for transmission of clinical SARS-CoV-2 isolates. We characterize tropism, respiratory tract replication and transmission of ancestral WA-1 compared to variants alpha (B.1.1.7), beta (B.1.351), gamma (P.1), delta (B.1.617.2) and omicron (B.1.1.529). We found that an index shedding threshold is a key determinant for viral transmissibility. Furthermore, we characterize two recombinant SARS-CoV-2 lacking either the ORF6 or ORF8 host antagonists. The removal of ORF8 shifts viral replication towards the lower respiratory tract, resulting in delayed and reduced transmission. Our results demonstrate the potential of our neonatal mouse model to characterize viral and host determinants of SARS-CoV-2 transmission, while revealing for the first time a role for an accessory protein this context. We now have a tractable small animal model to help us decipher and counteract some of the most decisive aspects of SARS-CoV-2 continued spread in the human population.

Introduction

Extensive genomic surveillance during the COVID-19 pandemic has provided granular detail on viral evolution in real-time. Despite worldwide vaccination efforts and increasing natural immunity, emerging SARS-CoV-2 variants continue to infect and burden the health of millions of people [1]. Past variants of concern include alpha (B.1.1.7), beta (B.1.351), gamma (P.1), delta (B.1.617.2) and omicron (B.1.1.529), while omicron sub-lineages BA.4.6, BA.2.75 and BF.7 currently dominate the second half of 2022 [2]. Variants differ in key genes across the viral genome, indicating specific selective pressures at work. These genes include Spike (*S*), *ORF1a*, *ORF1b*, Nucleocapsid (*N*) , *ORF3a*, *ORF6*, *ORF7a*, *ORF8*, *ORF9b*, Envelope (*E*), and Membrane (*M*). Much attention has been given to changes in Spike, as this envelope glycoprotein is the antigen targeted for most vaccination strategies to date and is key to viral entry into cells [3]. Variant-specific mutations in Spike's major antigenic sites have been linked to evasion from adaptive immunity [4-9]. Mutations in Spike's cleavage site modulate protease processivity during viral maturation, which in turn has been linked to changes within SARS-CoV-2's host tissue tropism (i.e. upper *versus* lower respiratory tract) and pathogenicity (i.e. milder or more severe) [10-12]. Mutations in Spike's ACE2 receptor binding domain may equally alter SARS-CoV-2's host tissue tropism, as well as potentially broaden the virus's host range by engaging ACE2 receptors of different species [13]. Other key hotspots that accumulate mutations in SARS-CoV-2 variants are accessory proteins, of which SARS-CoV-2 encodes 8, and some serve as antagonists of the antiviral host response, most notably type I interferon production and response [8, 14-19]. Our knowledge of SARS-CoV-2 ORFs stems from inferring functional similarities of well-studied antagonists encoded by SARS-CoV and other coronaviruses, and from limited functional studies using SARS-CoV-2 ORF cDNA overexpression constructs or recombinant SARS-CoV-2 [16-18, 20].

The high number of SARS-CoV-2 infections coinciding with the appearance of new variants raised concerns about enhanced transmission of these variants, posing considerable

ramifications for resolution of the COVID-19 pandemic [21]. During the early months of 2021, the alpha variant was considered to be 50% more transmissible than the other circulating lineages [22]. Early projections placed alpha as the dominant variant in the US by the spring of 2021, which was later confirmed by the increase of cases in the northern hemisphere with SARS-CoV-2 containing the alpha-defining mutations [22-24]. Initial studies on the beta variant reported its near complete dominance in Sub-Saharan Africa by the second half of 2020, as well as beta's ability to escape three classes of therapeutic monoclonal antibodies in addition to convalescent plasma therapy [25]. In the Amazonian region of Brazil, the gamma (P.1) variant was shown to be responsible for one of the early cases of reinfection [26], suggesting adaptive immune escape, and was estimated to be 1.7 to 2.4-fold more transmissible [27]. Later in 2021, during the second through the fourth quarter of the year, the delta and omicron variants emerged and rapidly dominated cases worldwide. Delta was shown to be shed at up to 1000 times higher titers than previously circulating variants, to be eight-fold less sensitive to vaccine-elicited antibodies compared with wild-type Wuhan-1, and to cause more severe pathology in humans [28-34]. The omicron variant was responsible for the steep increase of COVID-19 cases from late 2021 to early 2022, and multiple studies suggested it to be more transmissible than delta but to cause less lung pathology than other circulating variants, although this effect on pathology could be a result of the high percentage of immunized individuals at the time of infection [31, 35-39]. In addition, omicron evades adaptive immune responses more efficiently than any previous variants, as shown by a 44-fold reduced neutralization capacity of antibodies induced upon infection or vaccination with the BNT162b2 vaccine, which is based on the ancestral Wuhan-1 [31, 35-42]. Indeed, the continuous prevalence of the omicron variant throughout 2022 imposed a change in vaccine composition toward bivalent vaccines encoding Spike from both the ancestral Wuhan-1 and omicron lineages [43].

In addition to variant surveillance, the molecular characterization of SARS-CoV-2 variants is essential to our ability to develop appropriate antiviral strategies. Previous studies have characterized SARS-CoV-2 variants *in vitro* by evaluating receptor binding and affinity, antigenic escape and replication dynamics [4, 10, 13, 44-47] as well as *in vivo* regarding pathogenesis and immune evasion [11, 13, 48-61]. However, comparative studies on variant transmission and the molecular mechanisms governing transmission differences as a result of variant-specific mutations are still scarce, due to the difficulty with current models for SARS-CoV-2 transmission. While some individual aspects important for transmission, such as viral replication and immune antagonism can be studied *in vitro*, linking these findings to changes in transmission ultimately requires an animal model.

Currently available models for SARS-CoV-2 transmission include ferrets and hamsters, which are excellent models for pathogenesis. Ferrets display mild respiratory symptoms upon SARS-CoV-2 challenge, with high upper respiratory tract (URT) shedding, resulting in robust contact transmission but minimal aerosol transmission [62-65]. Hamsters are susceptible to SARS-CoV-2 infection and mostly develop mild disease with limited weight loss [53, 66-69]. They display a high but short peak of viral shedding, leaving a small window for transmission to occur [68, 69]. Despite this, both contact and aerosol transmission in most experimental hamster scenarios is 100 % effective, which complicates the assessment of suspected increased transmission by variants [68]. In addition, both the ferret and the hamster model lack the potential for genetic manipulation to address host determinants of transmission. Thus, it remains largely unclear which SARS-CoV-2 variant-specific mutations and which virus-induced host pathways contribute to transmission.

In contrast, mice are genetically tractable, and reagents are readily available; however, adult mice do not readily transmit respiratory viruses such as SARS-CoV-2 or influenza virus, a problem that has long stymied the field. To overcome this hurdle, we previously established a model for influenza virus transmission using neonatal mice of 4-7 days of age [70]. In contrast to

adult mice, the success of intra-litter virus transmission between pups is likely due to their 1. relative immune immaturity/tolerance towards infections, 2.reduced mobility, which increases contact between pups and/or 3. increased secretions during feeding by suckling. The mode of transmission in this model is a combination of direct contact and droplet transmission and, to a lesser extent, indirect contact (fomite) and aerosol transmission [70]. Although it has been successfully applied to study molecular mechanisms of influenza A virus transmission, the model is not established for other respiratory viruses, such as SARS-CoV-2.

Here, we present a neonate K18-hACE2 mouse model that allows for transmission of SARS-CoV-2 between pups of the same litter and examine side-by-side the transmission of early and current SARS-CoV-2 variants of concern (VOC). In addition, we characterize the transmission of two recombinant SARS-CoV-2, lacking accessory proteins ORF6 or ORF8. Our study showcases the power of our model to elucidate the dynamics of SARS-CoV-2 variant transmission and provides evidence of an accessory protein, ORF8, to be critical for SARS-CoV-2 transmission.

Results

Neonatal K18-hACE2 mice efficiently support SARS-CoV-2 WA-1 transmission

While influenza viruses readily infect wild-type mice, the ancestral SARS-CoV-2 and the clinically important delta variant rely on the human version of the SARS-CoV-2 host cell receptor, ACE2, and cannot engage murine Ace2 [47]. In contrast, a number of other SARS-CoV-2 variants acquired specific Spike mutations, most notably N501Y, which allows them to bind murine Ace2 [71]. Ultimately, we aimed to use our model to compare a panel of variants, from alpha to omicron, to the ancestral SARS-CoV-2. With this in mind, we developed our neonate model using K18-hACE2 mice, which express human ACE2 under the control of the K18 promoter [72].

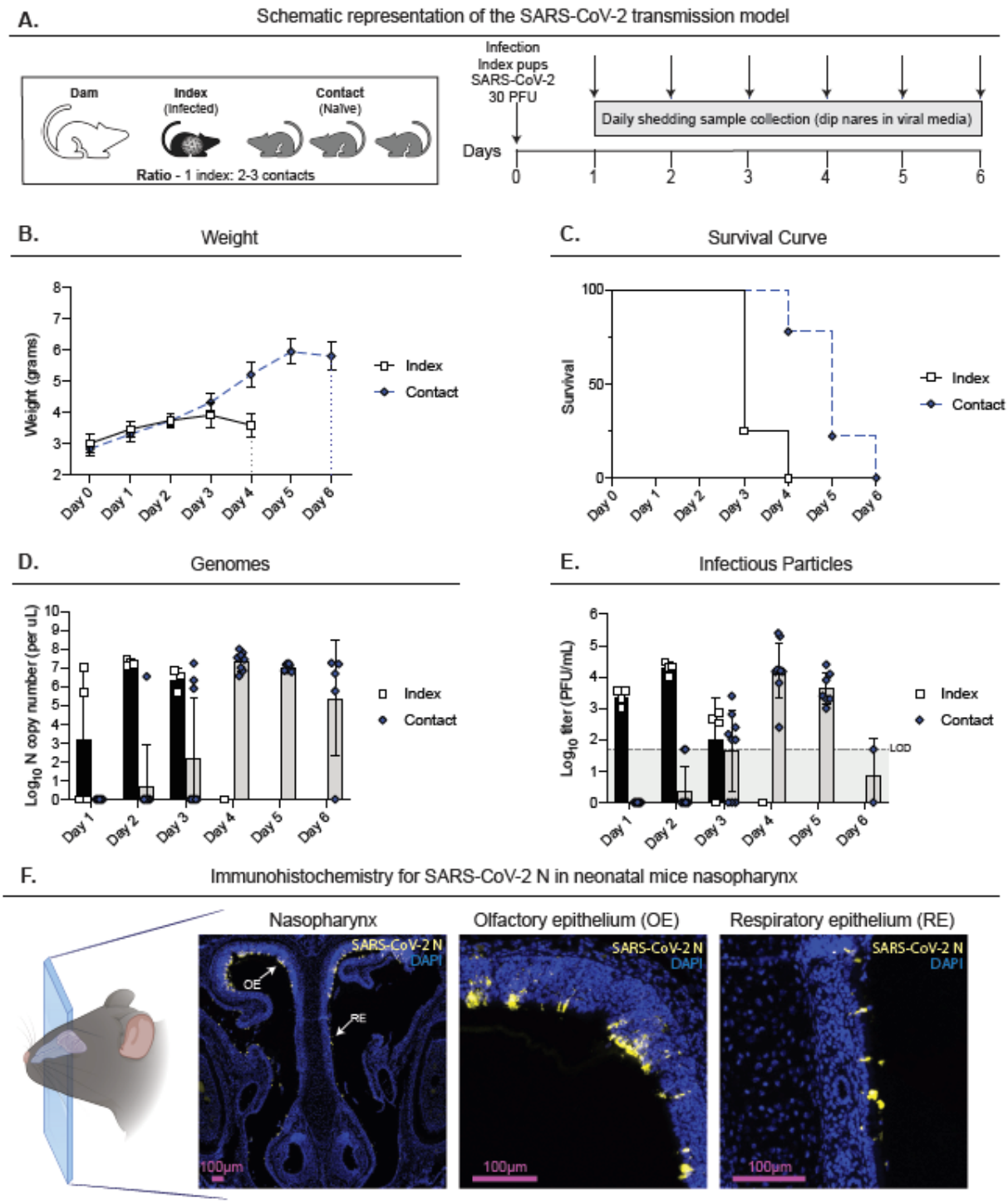

Figure 1. Establishment of a neonatal K18-hACE2 mouse transmission model (A) Schematic representation of the SARS-CoV-2 transmission model. At day 0 (4 to 7 days of age), K18-hACE2$^{+/-}$ pups were infected i.n. with 30 PFU of SARS-CoV-2 WA-1 (index) and cohoused with uninfected littermates (contact) for 6 days. Shedding of SARS-CoV-2 was collected by dipping the nares of each mouse in viral medium daily. (B) Average body weight curve of index and contact mice infected with SARS-CoV-2 WA-1. Error bars indicate SEM. Dotted lines represent last day of survival of each group. (C) Survival curve of index and contact mice after index infection with SARS-CoV-2 WA-1. (D and E) Shedding samples from each day were evaluated individually via RT-qPCR (D) or plaque assay (E). Each symbol represents the shedding titer measured from a single mouse on the specified day. Bars and error bars represent geometric mean and geometric standard deviation, respectively. Index and contact pups are shown by open or closed blue symbols, respectively. Data represents at least 2 independent repetitions. n = 4 - 6 contact mice per repetition. (F) At days 4-7 of age, pups were infected intranasally with 30 PFU of SARS-CoV-2 WA-1 and placed back with their mother for 2 days prior to sacrifice. Heads were fixed, paraffin embedded, sectioned through the nasopharynx, and stained for SARS-CoV-2 N protein (yellow) and DAPI (blue) for nuclei. Arrows represent areas magnified in the adjacent panels. OE - olfactory epithelium, RE - respiratory epithelium LOD - limit of detection

We combined C57BL/6 K18-hACE2$^{+/+}$ males and C57BL/6 (hACE2$^{-/-}$) females to produce SARS-CoV-2 WA-1 permissive K18-hACE2$^{+/-}$ offspring. At 4-7 days of age, index pups were infected intranasally with 3 µL of ancestral SARS-CoV-2 USA_WA-1/2020 (WA-1) without anesthesia and placed back with their naïve littermates to allow for intra-litter transmission (**Fig 1A**). A previous dose-response experiment revealed that 30 PFU of WA-1, as determined by plaque assay on VeroE6 cells (PFU_{VeroE6}), was the minimum dose to yield robust index infection (**Fig S1A**). Therefore, we used the infectious dose of 30 PFU_{VeroE6} for all subsequent transmission experiments. We monitored the pup's weight and survival daily and collected longitudinal shedding samples by dipping the pups' nostrils in PBS/0.3% BSA (**Fig 1A**). Our shedding assay allows the collection of nasal secretions from individual index and contact pups non-invasively, longitudinally, and without anesthesia. Thus, we leveraged the kinetics of upper respiratory tract (URT) shedding as a measure of viral infection.

Given that pups gain weight as they grow, we used the decrease in weight gain as a proxy for morbidity. Index pups failed to gain further weight by day 3 post-infection (3 dpi), and they all succumbed to infection by 4 dpi. (**Fig 1B, 1C**). Morbidity and mortality were offset in contact mice by 2-3 days compared to index mice, which was the first indication of transmission. We next analyzed nasal shedding samples for viral genomes by RT-qPCR. In index mice, we detected SARS-CoV-2 RNA as early as 1 dpi, whereas contact pups began shedding viral RNA from 2 dpi. (**Fig 1D**). A parallel experiment with heat-inactivated SARS-CoV-2 showed that the genomes present in shedding samples were due to active viral replication and not carryover from inoculates (**Fig S1B**). Detecting SARS-CoV-2 RNA in contact mice was thus another indication of transmission. However, we conservatively define transmission as the detection of viral infectious particles in contact mice. Therefore, we next determined viral titers in nasal shedding samples by performing a plaque assay on VeroE6 cells overexpressing ACE2 and TMPRSS2. These cells are more permissive to SARS-CoV-2 and increase the sensitivity of the plaque assay to allow the detection of low viral titers [73, 74]. Infectious particles from index

mice (**Fig 1E**) correlated with the onset of RNA detection (**Fig 1D**) but decreased by day 3, contrasting ongoing elevated RNA levels. In contact pups, infectious particles peaked on day 4 and decreased by days 5 and 6, whereas viral RNA remained elevated. Of note, all contact pups shed infectious particles by day 4, representing 100% transmission efficiency of WA-1 in our model.

Detection of infectious particles in shedding samples of K18-hACE2 neonatal mice suggested robust viral infection in the URT. To determine the sites of infection within the URT, we performed immunohistochemistry on the nasopharynx of index pups. Neonatal mice were infected with 30 PFU_{VeroE6} of SARS-CoV-2 WA-1; the heads were harvested at their peak of viral shedding (2 dpi), sectioned through the nasopharynx, and stained for SARS-CoV-2 N protein. SARS-CoV-2-positive cells were detected in the upper olfactory and respiratory epithelium lining, demonstrating replication of SARS-CoV-2 WA-1 in cells of the URT (**Fig 1F**). Taken together, these results establish and validate a tractable neonatal K18-hACE2 mouse model for the transmission of SARS-CoV-2.

SARS-CoV-2 variants of concern display distinct replication dynamics and tropism in neonatal index mice

Viral transmission is determined by multiple factors, including index viral URT titers, efficiency of infectious viral particle expulsion from the index, and the susceptibility to infection of the exposed contact [70, 75]. For SARS-CoV-2, in humans the predominant transmission route is via respiratory droplets, which is heavily influenced by viral tropism towards the URT that favors the expulsion of infectious viral particles into the environment [76]. Indeed, the high transmissibility of some variants, namely alpha and delta, has been proposed to be linked to their success in efficient URT replication [31, 59, 77].

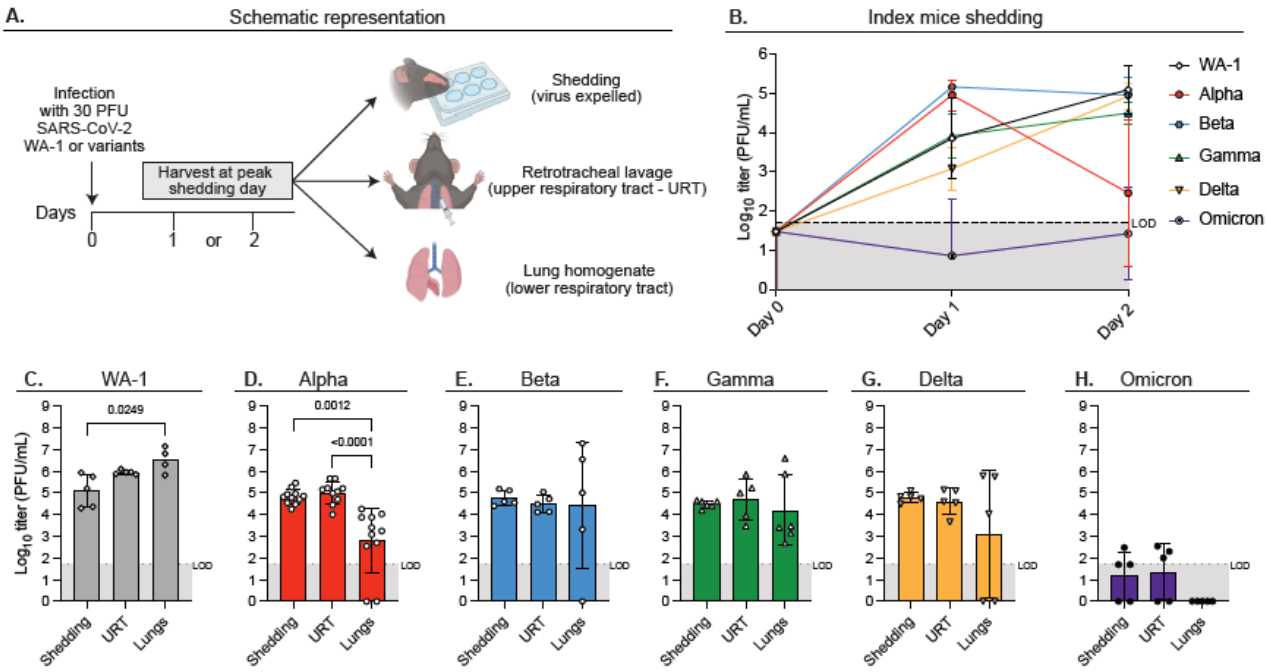

Figure 2: SARS-CoV-2 variant replication dynamics and tropism in index mice. (A) Schematic representation of the experiment. At day 0 (4 to 7 days of age), K18-hACE2$^{+/-}$ pups were infected i.n. with 30 PFU of either SARS-CoV-2 WA-1 or the variants of concern alpha, beta, gamma, delta or omicron, collected shedding samples at days 1 and 2 and determined the peak day of viral shedding for each variant. At their peak day of viral shedding, we performed a retrotracheal lavage for the upper respiratory tract, and collected lung homogenate for the lower respiratory tract to quantify the amount of infectious virus via plaque assay. (B) Index mice shedding titers at days 1 and 2pi. Symbols represent geometric mean with geometric standard deviation.Data represents at least 2 independent repetitions with n = 6 - 15 index per group. Shaded gray area represents values below detection level (C - H) Viral titers of mice infected with either (C) WA-1, (D) alpha, (E) beta, (F) gamma, (G) delta or (H) omicron in different compartments. Each symbol represents the shedding titer measured from a single mouse while bars and error bars represent geometric mean and geometric standard deviation, respectively. Numbers represent p-values of Kruskal-Wallis test. Only significant values are presented. LOD: limit of detection.

To characterize SARS-CoV-2 variant tropism and replication dynamics, we first generated clonal (plaque-purified), sucrose-purified, and deep-sequenced viral working stocks. This rigorous quality-control pipeline ensured the identity of VOCs, the lack of tissue culture-induced mutations, and the purity of inoculates (i.e. the lack of cell debris or inflammatory cytokines from producer cell supernatants). We then infected K18-hACE2$^{+/-}$ index mice with 30 PFU_{VeroE6} of either SARS-CoV-2 WA-1, B.1.1.7 (alpha), B.1.1.351 (beta), P.1 (gamma), B.1.617.2 (delta) or B.1.1.529 (henceforth referred to as omicron BA.1). We first collected shedding samples on 1 and 2 dpi to determine the peak day of viral shedding for each virus (**Fig 2A, B**). Shedding from mice infected with alpha and beta peaked at 1 dpi and decreased by 2 dpi, while shedding of ancestral WA-1, gamma, and delta peaked at 2 dpi, before decreasing by 3dpi (data not shown). Mice infected with omicron expelled low levels of virus, with most replicates below the detection limit and just one replicate at 2 x 10^3 PFU/mL at 1 dpi.

To characterize viral tropism for each variant in more detail, we next measured infectious particles in shedding samples (representing expelled virus), in retrotracheal lavages (representing virus present in the upper respiratory epithelium), and in lung homogenates (representing virus present in the lower respiratory tract). We collected these samples at the respective peak day of shedding as determined in Figure 2B, and quantified the amount of infectious virus particles by plaque assay on Vero E6 ACE2 TMPRSS2 (**Fig 2A**). We found the distribution of viral load in these sample types to be distinct for specific viruses (**Fig 2C-2H**). For WA-1, expelled virus titers were an average of 10^5 PFU/mL, with comparable levels in the URT, but significantly higher titers ($5x10^6$ PFU/mL) in the lungs, suggesting that in our model, at peak replication, WA-1's tropism progresses towards the lower respiratory tract (**Fig 2C**). For alpha, expelled virus titers and URT titers were comparable in magnitude to WA-1, at 10^5 PFU/mL, but lung titers were significantly lower at 10^3 PFU/mL. (**Fig 2D**). This suggests that in our model, at peak shedding day, alpha replication favors the URT. For beta and gamma, we found no significant differences in titers between expelled virus, URT, and lungs, suggesting equal ability to infect and replicate in both the URT and the lower respiratory tract, and to be expelled from the URT (**Fig 2E, 2F**). Infectious titers in the three sample types reached 10^5 PFU/mL, which is comparable to shedding and URT replication of WA-1 and alpha. For delta, infectious titers in the shedding and URT were comparable to the levels of the aforementioned variants, but we observed a broad distribution in the lungs, with some pups displaying higher viral titers in the lung than in shedding or URT (**Fig 2G**). Finally, and as expected from the shedding samples, we found low omicron titers in the URT, and no infectious virus was detected in the lungs, suggesting that this variant might not replicate efficiently in neonatal K18-hACE2 mice. Our results are in line with findings from others, showing that the omicron BA.1 variant is attenuated in adult mice and hamsters [48, 55, 61]. Of note, viral loads in all shedding samples were similar to those from their respective retrotracheal lavage samples, showing that 1. viruses assayed do not seem to have a defect in viral expulsion and that 2. in this model, URT shedding can be

used as a proxy for URT replication. Taken together, our results demonstrate that, except for omicron, our model allows for efficient replication and shedding of different SARS-CoV-2 VOCs at comparable levels to the ancestral WA-1. We find a significant preference for alpha to replicate in the URT, and no replication preference for beta, gamma, and delta between URT and lower respiratory tract. Temporal shedding dynamics differ between variants, which we hypothesize is a result of the differences observed in viral tropism and allows this model to be used as a tool to understand the mechanisms of variant SARS-CoV-2 transmission.

Neonatal mouse model reveals dynamics in SARS-CoV-2 variant transmission

We next utilized our neonatal mouse model to test transmission of our panel of SARS-CoV-2 variants ranging from early to current pandemic isolates. We infected 4-7-day-old index K18-hACE2$^{+/-}$ transgenic mice intranasally with 30 PFU_{VeroE6} of either ancestral SARS-CoV-2 WA-1 or alpha, beta, gamma, delta or omicron BA.1 and cohoused them with naïve neonatal mice at a 1:6-9 ratio. Each day, we monitored weight and mortality as described above (**Fig S2**).

Index mice infected with alpha and beta variants started to lose weight at 2 dpi, before succumbing to infection at 3 dpi, similar to WA-1 (**Fig S2A-S2C**). In contrast, index mice infected with delta and gamma continued to gain weight until they succumbed to infection at days 3 and 4, respectively (**Fig S2D and S2E**). Index mice infected with the omicron variant started to lose weight by 3 dpi and succumbed to infection by 5 dpi (**Fig S2F**), despite the low viral burden in shedding samples and retrotracheal lavages (**Fig 2H**). These results shows that index mice do get infected with omicron BA.1; however, in alignment with previous studies in adult mice and hamsters, omicron BA.1 has delayed pathogenicity in our model [55].

Except for omicron, and in a similar manner to WA-1 (**Fig 1B**), contact mice in cages with other variants succumbed to infection (**Fig S2**). By 7 dpi, contact mice of alpha and delta infections displayed 100% mortality, while contact mice of WA-1, beta and gamma infections showed a mortality rate of 75%, 86%, and 56%, respectively. This indicated that our model captured

differences in the transmission of SARS-CoV-2 variants, which led us to investigate the dynamics of viral shedding in the index and contact mice.

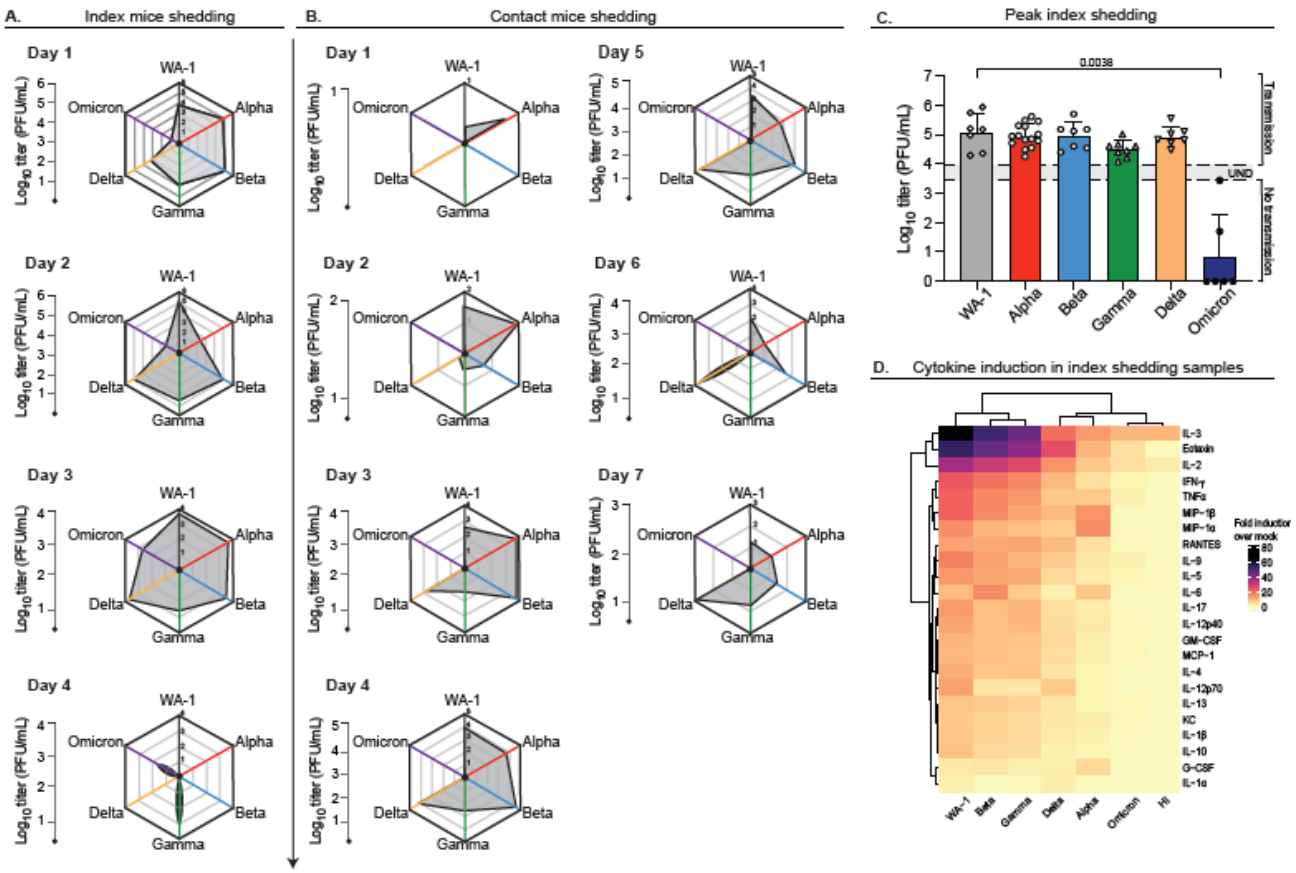

Figure 3: SARS-CoV-2 neonatal model reveals variant transmission dynamics.(A and B) Spider plots representing viral titers of shedding collected from (A) index or (B) contact mice infected with SARS-CoV-2 variants. At day 0 (4 to 7 days of age), K18-hACE2$^{+/+}$ pups were infected i.n. with 30 PFU of SARS-CoV-2 variants (index) and cohoused with uninfected littermates (contact) for 7 days at a ratio of 1 index to 6-9 contacts. Shedding of SARS-CoV-2 was collected by dipping the nares of each mouse in viral medium daily. Colored axes represent index or contact mice infected with each variant, while the shaded gray area corresponds to the geometric mean of viral titers detected in the shedding sample via plaque assay. Gray lines and numbers denote Log_{10} of PFU per milliliter. Data represents at least 2 independent repetitions with n = 2-4 index and n = 6-9 contacts per group (C) Peak index shedding titers of mice infected with SARS-CoV-2 variants. Each symbol represents the shedding titer measured from a single mouse while bars and error bars represent geometric mean and geometric standard deviation, respectively. Numbers represent p-values of Kruskal-Wallis test. Only significant values are presented. UND: undertermined (D) Heatmap representing cytokine induction in shedding samples of index mice infected with SARS-CoV-2 variants or HI SARS-CoV-2 at day of peak titer. Colors represent fold induction over mock-infected pups.

Because index shedding is an important factor determining transmission, we next investigated the dynamics of viral shedding in index mice longitudinally to determine if differences in index shedding of SARS-CoV-2 variants correlated with transmission efficiency (**Fig S3, Fig 3A, 3B** and **Table 1)**. Viral shedding of index pups infected with alpha had the highest titers at 1 dpi, whereas WA-1, beta, delta, and gamma's shedding titers were highest at 2 dpi (**Fig S3, Fig 3A**). At 4 dpi, only data points for omicron and gamma remain, as mice infected with the other variants had succumbed to infection (**Fig S2D, S2F**).

Table 1. Parameters of SARS-CoV-2 variant transmission in the K18-hACE2 neonatal model

SARS-CoV-2	Percentage of infected contact	Time to 1st contact infection (above LOD)	Time to all contact infection	Time of peak PFU in contact mice	Maximum peak contact titer (PFU/mL)	Average pe contact tit (PFU/mL)
WA-1	100% (12/12)	2 days	4 days	4 days	4.40×10^5	1.01×10^5
Alpha	100% (27/27)	1 day	4 days	4 days	8.00×10^5	9.30×10^4
Beta	100% (14/14)	2 days	3 days	4 days	7.00×10^5	1.44×10^5
Gamma	94% (15/16)	2 days	N/A	4 days	1.35×10^6	1.54×10^5
Delta	100% (13/13)	2 days	4 days	4 days	3.50×10^5	6.35×10^4
Omicron	0% (0/8)	N/A	N/A	N/A	0	0

To capture the kinetics of transmission to contact pups, daily shedding of contact mice was used as a proxy for successful viral acquisition and replication. Interestingly, alpha was present in contacts as early as 1 dpi, whereas WA-1, beta, gamma, and delta were first detected above the LOD at 2 dpi, and omicron did not transmit in this model. This timing of viral transit from index to contacts suggested that expelled virus from the index pup during its peak titer corresponded the timing of virus acquisition by the contacts. For example, alpha-infected index pups shed highest at 1 dpi, and correspondingly, the virus was detected in contacts the same day. The same was true for WA-1, beta, gamma, and delta, where index-infected pups shed highest at 2 dpi, and detection in contacts was achieved the same day. In all, our data suggest that alpha transmits the fastest among the variants tested, and that the timing of virus detection in contacts can be predicted by the timing of peak viral shedding titer of the index pups.

In contrast to time-to-first virus detection in contacts, transmission efficiency did not correspond with peak index shedding titers. We observe complete (100%) transmission for WA-1, alpha, beta, and delta, a slightly reduced transmission (94%) for gamma, and (0%) for omicron (**Tab 1**). Despite the fact that omicron-infected index pups shed virus consistently for 3 days, the maximum index shedding titer is much lower compared to other variants that displayed successful transmission. Our results are similar to observations in the hamster model for SARS-CoV-2 transmission (personal communication by Yoshi Kawaoka, Jacco Boon, and other NIAID

SAVE investigators). This suggests that an index shedding titer threshold likely exists in this model that may predict transmission success to contacts.

We next defined the minimum index shedding threshold required for productive SARS-CoV-2 transmission in our model (**Fig. 3C**). The threshold is equal to or above 1.2 x 10^4 PFU/mL, which was the lowest titer obtained at the peak shedding day among WA-1, alpha, beta, gamma, and delta variants. Using omicron as a non-transmitter, we define that index shedding titers at or below 2.7 x 10^3 PFU/mL would likely not allow for transmission in our model. While these thresholds may allow for a prediction of a variant's transmission potential based on index mice shedding, it is important to note that in experimental conditions with additional transmission bottlenecks, such as adaptive immune status of the index and/or contact mice, the thresholds are likely different.

An antiviral/inflammatory response to infection is expected to attenuate the virus within the host, causing reduced transmission [75, 78]. However, increased inflammation may also induce URT secretions that help expel the virus into the environment, which may favor transmission [79, 80]. Several studies have shown that SARS-CoV-2 variants induce differential inflammatory repertoires, but limited information is available regarding inflammatory markers in the URT and the contribution of specific inflammatory signatures to transmission [53, 58, 81]. In order to link a variant's URT inflammatory repertoire with its transmission potential, we analyzed the cytokines present in the URT shedding samples of neonatal mice infected with SARS-CoV-2 variants. We first validated our system by intranasally inoculating neonatal mice with either heat-inactivated (HI) SARS-CoV-2 WA-1, SARS-CoV-2 WA-1, or poly (I:C). We collected shedding samples at 6 and at 48 hours post-infection (hpi), and analyzed them by multiplex ELISA. We detected the highest overall cytokine signature in samples from animals infected with SARS-CoV-2, suggesting that active viral replication is required to induce a robust cytokine response (**Fig S1C**). IL-3, Eotaxin, and IL-2 were the most upregulated cytokines upon WA-1 infection

compared to PBS-inoculated animals, aligning with previously reported data of cytokine upregulation in the lower respiratory tract upon SARS-CoV-2 infection [82, 83].

We next infected neonatal mice with either HI SARS-CoV-2, SARS-CoV-2 WA-1 or SARS-CoV-2 variants alpha, beta, gamma, delta, and omicron, and measured cytokines in shedding samples at their respective day of peak viral replication (**Fig 3D**). Of note, on that day, average viral titers were comparable, between 10^4 and 10^5 PFU/mL, except for omicron BA.1, which was 10^1 PFU/mL (**Fig 3C**), allowing for qualitative comparison of cytokine signatures between equally replicating viruses. Indeed, the cytokine signature for omicron was most similar to that of HI SARS-CoV-2 (**Fig 3D**), likely reflecting the poor replication of omicron BA.1 in our model (**Fig 2B, 2H, 3C**). For equally replicating viruses WA-1, alpha, beta, gamma, and delta we found that cytokine signatures did not generally correlate with their transmission dynamics. WA-1, beta, and gamma infections, whose transmission differed in terms of onset, time to completion, and level of completion (**Tab 1**), resulted in overall similar cytokine responses (**Fig 3D**). Beta and gamma signatures were overall more similar to each other than to WA-1. For instance, IL-3, Eotaxin, IL-2 and IFN-γ were the most prominently present cytokines after infection with these three viruses (**Fig 3D**), while IL-6 was induced to higher levels upon beta infection as opposed to any other viruses.

In contrast, delta and alpha infections yielded a response more similar to those of omicron and HI virus and were most similar to each other, with an overall lower magnitude of cytokine induction compared to the cluster formed by WA-1, beta, and gamma. Despite the robust replication of alpha, its cytokine signature is notably quiet, highlighting the previously reported efficiency of this variant in evading innate detection mechanisms [6]. Interestingly, WA-1 and alpha, which were most similar viruses in terms of transmission onset (1 dpi), time to completion (4 dpi), and achievement of completion (100%), were notably different in terms of cytokine profile from each other, suggesting that index cytokine responses during its peak shedding titer

does not correspond with the virus' transmission dynamics, indicated that perhaps, different viruses induce cytokine responses to achieve their transmission in different ways.

Taken together, our results show that, except for omicron BA.1, our neonatal mouse model is able to reveal the transmission dynamics inherent to the SARS-CoV-2 variants. Our non-invasive method of viral sampling enables tracking viral replication in individual index and contact mice over time, providing unprecedented granularity in transmission parameters, including the characterization of variant-specific cytokine signatures.

Accessory proteins ORF6 and ORF8 play a role in successful SARS-CoV-2 transmission

Inarguably, the SARS-CoV-2 protein undergoing the most dramatic evolution during the COVID-19 pandemic is spike. This is likely due to the selection of spike mutations that lead to a refinement of human receptor binding [13, 46, 47] and/or evasion of increasing adaptive immunity to SARS-CoV-2, either by vaccination or natural immunity [58, 84, 85]. In addition to mutations in spike, a number of variants also display mutations in accessory genes, such as ORF3, ORF6, ORF7, and ORF8, which have been implicated in the interference of immune signaling or direct host effector counteraction [16, 60]. The selective advantage of changes in these accessory proteins remains largely undefined. Previous studies used recombinant SARS-CoV-2 lacking specific accessory proteins to characterize their role in viral replication and pathogenesis in adult K18-hACE2 mice. Of interest, mice infected with recombinant SARS-CoV-2 lacking ORF8 resulted in increased lung pathology in one study [86], and 100% mortality in another study [60], underscoring the importance of accessory proteins in reducing SARS-CoV-2 inflammation and modulating host response. To our knowledge, to this date, the role of SARS-CoV-2 accessory proteins specifically in transmission has not been studied. We thus aimed to determine how the lack of specific accessory proteins impacts SARS-CoV-2 transmission in our model. We focused on two accessory proteins: ORF8, which has mutations defining the alpha, gamma, and delta variants, and, ORF6, which lacks mutations in the variants utilized in this

study but is mutated in other Omicron variants (BA.2, BA.2.12 and BA4) in addition to being one of the best-characterized SARS-CoV-2 accessory proteins [8, 14, 17, 60, 87] (**Fig 4A**).

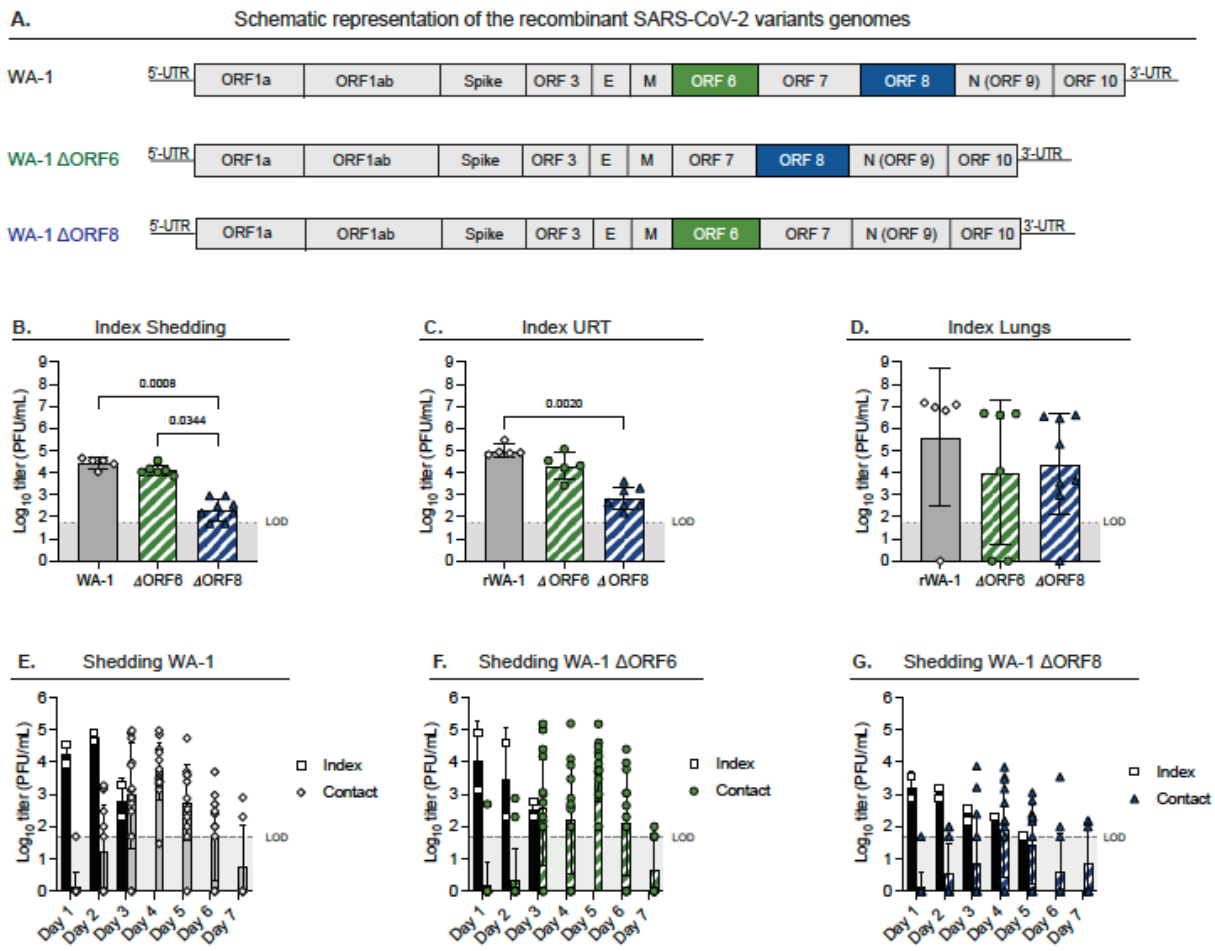

Figure 4. Characterization of replication and transmission of ΔORF6 and ΔORF8 viruses (A) Schematic representation of the recombinant SARS-CoV-2 viruses. (B - D) Viral titers of index mice infected with 30 PFU of either WA-1, WA-1 lacking ORF6 (WA-1 ΔORF6) or WA-1 lacking ORF8 (WA-1 ΔORF8) in (B) shedding, (C) upper respiratory tract or (D) lungs. Each symbol represents the shedding titer measured from a single mouse while bars and error bars represent geometric mean and geometric standard deviation, respectively. Numbers represent p-values of Kruskal-Wallis test. Only significant values are presented (E - G) Viral titers of daily shedding samples of index and contact mice infected with SARS-CoV-2 recombinant variants via plaque assay. At day 0 (4 to 7 days of age), pups were infected i.n. with 30 PFU of SARS-CoV-2 recombinant variants (index) and cohoused with uninfected littermates (contact) for 7 days. Shedding of SARS-CoV-2 was collected by dipping the nares of each mouse in viral medium daily. Each symbol represents the shedding titer measured from a single mouse on the specified day. Index pups are shown by open squares and black bars, while contact mice are represented by white (E) or colored symbols (F,G) and grey (E), green patterned (F) or navy patterned (G) bars. Bars denote geometric mean with geometric standard deviation. LOD: Limit of detection

We infected K18-hACE2$^{+/-}$ neonatal mice with 30 PFU$_{VeroE6}$ of recombinant SARS-CoV-2 WA-1, SARS-CoV-2 lacking ORF6 (WA-1 ΔORF6), or SARS-CoV-2 lacking ORF8 (WA-1 ΔORF8), and at 2 dpi collected shedding samples (expelled virus), retrotracheal lavage fluids (URT replication) and lungs (lower respiratory tract replication) to quantify the amount of infectious virus via plaque assay (**Fig. 4B-D**). Similar to our previous observations with the WA-1 isolate

(**Fig 2C**), we observed a trend of higher titers of recombinant SARS-CoV-2 WA-1 in the lung homogenates, $5x10^5$ PFU/mL, and lower titers in the URT and shedding samples, at $1x10^5$ or $5x10^4$ PFU/mL, respectively (**Fig 4-D**). For WA-1 ΔORF6, we obtained similar titers in all three sample types, $1x10^4$ PFU/mL on average, although there was a broad distribution with some pups displaying higher viral titers in the lung than in shedding or URT samples. We concluded that, in our model, the lack of ORF6 did not attenuate viral replication or significantly change tissue tropism with respect to parental WA-1. This was different for ORF8. WA-1 ΔORF8 expelled virus loads and URT virus loads were $5x10^2$ or $1x10^3$ PFU/mL, respectively, and thus significantly lower than for WA-1 or WA-1 ΔORF6. In contrast, lower respiratory tract burden was comparable to those of WA-1 and WA-1 ΔORF6, an average of $5x10^4$ PFU/mL. Thus, the lack of ORF8 seems to significantly change tissue tropism away from the URT and towards the lower respiratory tract. To our knowledge, this is the first report of ORF8's role in SARS-CoV-2 tropism.

We next performed transmission experiments with the three recombinant viruses. We infected 4-7-day-old index K18-hACE2$^{+/-}$ transgenic mice intranasally with 30 PFU_{VeroE6} of either SARS-CoV-2 WA-1, SARS-CoV-2 WA-1 ΔORF6, or SARS-CoV-2 WA-1 ΔORF8, cohoused them with naïve neonatal mice at a 1:6-9 ratio and analyzed the expelled virus titers from individual index and contact mice longitudinally. Similar to the WA-1 isolate (**Fig 2B**), recombinant WA-1 index shedding titers peaked at 2 dpi, and then decreased before the index pups succumbed to infection at 4 dpi (**Fig 4E**). Again, similar to the WA-1 isolate, recombinant WA-1 transmission first occurred at day 1 pi, was complete by 4 dpi, and contact shedding titers decreased from 5dpi onwards (**Fig 4E, Tab 2**). In contrast, WA-1 ΔORF6 index shedding titers peaked earlier, at 1 dpi and steadily decreased until 3 dpi before the pups succumbed to infection (**Fig 4F**). Similar to parental recombinant WA-1, transmission of WA-1 ΔORF6 first occurred at 1 dpi, but despite the earlier peak in index replication, complete WA-1 ΔORF6 transmission was only achieved at 5 dpi (**Fig 4F, Tab 2**). Peak contact titers of WA-1 ΔORF6 infection were also delayed to 5 dpi,

as opposed to 4 dpi for WA-1, even though the contact shedding titers decreased from 6 dpi until 7 dpi, similarly to the parental WA-1 infection (**Fig 4E, 4F**). Together, these results suggest that the delay in transmission may be a reflection of a slight viral attenuation due to the lack of ORF6, the latter of which has been reported elsewhere [87].

Similar to WA-1 ΔORF6, WA-1 ΔORF8 index shedding titers also peaked at 1 dpi, albeit at a lower level. In contrast to both parental WA-1 and WA-1 ΔORF6, infectious virus in index mice was still detectable by 5 dpi, suggesting slower viral clearance in the absence of ORF8 (**Fig 4G**). Onset of transmission for WA-1 ΔORF8 was similar to WA-1 and WA-1 ΔORF6, 1 dpi, but in contrast to the other two recombinant viruses, transmission was incomplete until the experiment ended at 7 dpi. We hypothesize that this reduction in transmission is a consequence of the low and declining viral loads expelled by the index mice. In addition, the maximum viral titer detected in WA-1 ΔORF8 contact mice was 7.5 x 10^3 PFU/mL which is lower than the 1.5 x 10^5 PFU/mL observed with WA-1 ΔORF6 or the 9.5 x 10^4 PFU/mL observed with the parental WA-1 (**Tab 2**). This was the first time that we observed such low shedding titers in contact pups, except for omicron BA.1, as other SARS-CoV-2 variants showed contact titers of 10^4-10^5 PFU/mL. Taken together our results show how removal of one SARS-CoV-2 accessory protein, ORF8, shifts viral tropism towards the lower respiratory tract, resulting in reduced transmission.

Table 2. Parameters of SARS-CoV-2 recombinant virus transmission in the K18-hACE2 neonatal model

SARS-CoV-2	Percentage of infected contact	Time to 1st contact infection	Time to all contact infection	Time of peak PFU in contact mice	Maximum peak contact titer (PFU/mL)	Average peak conta titer (PFU/mL)
WA-1	100% (13/13)	1 day	4 days	3 days	9.50 x 10^4	1.94 x 10
WA-1 ΔORF6	100% (14/14)	1 day	5 days	5 days	1.55 x 10^5	2.04 x 10
WA-1 ΔORF8	92% (12/13)	1 day	N/A	3 days	7.50 x 10^3	7.28 x 10

Discussion

Epidemiological studies suggest that some mutations inherent to the SARS-CoV-2 variants result in increased transmissibility [35, 88, 89]. Evasion from increasingly immune populations due to previous infection or immunization, leading to unhampered URT replication and transcending to effective transmission despite population immunity may be one explanation for this phenomenon. Apart from adaptive immune evasion, molecular determinants for increased variant transmissibility remain largely unknown and their study requires the use of animal models with immune naïve individuals.

Mouse models of SARS-CoV-2 infection have been utilized extensively to study the pathogenesis of emerging SARS-CoV-2 variants [13, 48, 56, 60, 61, 82, 90, 91]. However, adult mice do not readily transmit SARS-CoV-2. In our study, we developed and validated a neonatal mouse model to characterize the transmission of SARS-CoV-2 based on our previous experience with influenza A virus (Fig. 1, [70]). Using a unique SARS-CoV-2 panel spanning early to current pandemic isolates, we demonstrate how variant-inherent mutations affect tropism and shedding (Fig 2), transmission (Fig 3), and upper respiratory tract cytokine repertoires (Fig 3). Finally, our study reveals a previously unappreciated role for the accessory protein ORF8 in viral upper respiratory tract tropism and transmission (Fig 4), showcasing the power of our model to study the molecular determinants of SARS-CoV-2 transmission.

Respiratory viral transmission is determined by viral infectivity, the magnitude of the viral load shed from the initially infected individual, the susceptibility to infection of the exposed contact to infection, the exposure route between index and recipient, and environmental factors that can impact viral particle stability and infectivity during transmission [75, 92]. In humans, SARS-CoV-2 is shed from an infected person and transmitted to bystanders mainly by respiratory droplets [93, 94]. This ability to shed virus is driven by productive viral replication in both the upper and

lower respiratory tract [76]. The ancestral SARS-CoV-2 WA-1 displays a gradient of infectivity from the human proximal to the distal respiratory tract, driven by the infection of ciliated airway cells and alveolar type 2 cells expressing ACE2 and TMPRSS2 [95, 96]. These cells and the expression of these two host factors show different distributions in the URT versus the lower respiratory tract [97-100] and can thus drive tropism to either site by allowing for different entry routes. SARS-CoV-2 enters cells via either of two routes: the endosomal pathway, which requires engagement of the ACE2 receptor and spike protein processing in the endosome by cathepsin L, or the cell surface pathway, which also relies on engagement of ACE2 but spike processing occurs on the plasma membrane by TMPRSS2 [101]. Spike mutations E484K, K417N/T, N501Y, and P681H/R are found in a number of SARS-CoV-2 VOCs and have been shown to alter host receptor binding affinity [13, 46, 47], to promote viral immune evasion [58, 84, 85], and to shift the viral entry route by altering spike protein processing via the S1/S2 cleavage site [4, 45, 46, 102]. Indeed, a recombinant SARS-CoV-2 lacking the polybasic furin S1/S2 cleavage site was shed to lower titers from the URT of ferrets and was thus not transmitted to cohoused sentinel animals [65]. Similarly, in hamsters, deletion of the polybasic furin S1/S2 cleavage site resulted in a lower viral burden in nasal turbinates, trachea and lungs of index hamsters, thereby reducing direct contact transmission [103]. The authors propose that the polybasic cleavage site shifts viral entry away from cathepsin and towards the TMPRSS2-dependent pathway and allows the virus to avoid IFITM proteins, which are potent endosomal restriction factors inhibiting viral membrane fusion While these studies were performed with a recombinant SARS-CoV-2, it is conceivable that variant-inherent natural spike mutations similarly alter SARS-CoV-2 entry routes, resulting in a change in viral tropism, followed by differential shedding from the URT and, ultimately, a shift in viral transmission. Indeed, we observed in previously published work that mice infected with the alpha variant, which carries a P681H substitution at the S1/S2 cleavage site that increases cleavage by furin-like proteases [10], displayed a lower viral burden in the lungs as compared to the URT. Conversely, mice

infected with WA-1 showed a higher viral burden in the lungs than in the URT. This might suggest that WA-1 favors replication in the lower respiratory tract, resulting in a reduced viral load compared to other variants that preferentially replicate in the URT. Surprisingly, even though alpha and delta-infected mice displayed lower titers in the lungs, the average viral load shed from alpha, delta, and WA-1 infected mice was comparable between variants. Given that alpha was transmitted earlier than WA-1 and that both viruses shed at comparable levels while having a difference in tropism, we hypothesized that in our model, URT favorability alone does not necessarily drive more rapid transmission.

The efficiency of viral expulsion from the URT is another factor determining respiratory virus transmission [104]. Pathogen shedding can be shaped by URT local immune responses, which can either reduce transmission by attenuating replication via inflammatory responses or, and somewhat counterintuitively, promote nasal secretions to enhance transmission [78, 79]. In humans, proinflammatory cytokines are associated with prolonged viral RNA shedding [105] and some SARS-CoV-2 variants have been shown to be shed for longer periods of time [29]. It is plausible that a variant's inflammatory repertoire determines its transmission potential, since variant-inherent mutations trigger differential immune responses that influence viral shedding [58, 81]. In our study, however, we did not observe a positive correlation between viral shedding and cytokine induction in the nasal secretions of mice infected with SARS-CoV-2 variants. Mice infected with WA-1 and alpha replicated to similar levels in the URT and were also expelled to similar levels; yet, their cytokine signatures were different, with WA-1 showing elevated cytokine levels while alpha's quieter signature was comparable to that of heat-inactivated virus. This result concurs with recent data highlighting alpha's ability to successfully evade the innate immune system detection mechanisms [6]. Mice infected with delta also showed a quieter signature than WA-1, beta, or gamma, which could be a consequence of differences in tropism and viral replication, driven at least in part by the P681H/R mutation, or a reflection of differential

immune antagonism. This data demonstrates that there are multiple parameters that determine efficient SARS-CoV-2 transmission that can potentially be experimentally untangled in our model.

The omicron variant challenges the validity of small animal models for SARS-CoV-2. Despite its success in human populations, and similar to what we report here, several studies found severe attenuation of omicron in mice and hamsters [48, 52, 54, 55, 61]. Of note, there is discrepancy in the literature, as other studies report robust omicron replication in these models [13, 56, 86]. It has been proposed that omicron is the SARS-CoV-2 variant with the highest adaptation to humans [106]. Although the mechanisms for omicron's attenuation in rodents remain unknown, this adaptation could be through mutations in spike, that alter receptor binding and spike processing, and/or specific mutations in accessory proteins, such as ORF1a:L3674-, S3675-, G3676-, ORF1b: P314L and ORF9b: E27-,N28-, A29, that could affect replication, cell and tissue tropism, and the induction of inflammatory responses [4, 39, 47, 48, 50]. Additional studies are needed to elucidate these mechanisms and develop an adapted model to study omicron pathogenesis and transmission.

In our system, except for omicron, we observed very high SARS-CoV-2 variant transmission (above 90%), yet, our method was granular enough to detect subtle differences between variants. We speculate that transmission differences between SARS-CoV-2 variants may have been more dramatic under adaptive immune pressure. For this study, we chose naïve animals, which allowed us to reveal specific aspects driving SARS-CoV-2 variant transmission. In future studies, we plan to examine the effects of varying adaptive immune pressures. In particular, we can vaccinate dams prior to pregnancy, so pups will receive immunoglobulins via transplacental passage or breastfeeding, which has been shown to reduce transmission in our influenza A virus model [70].

Lower inflammatory signatures of alpha and delta could be due to enhanced innate immune antagonism driven by their accessory proteins [107]. ORFs encoding these accessory proteins have accumulated specific mutations in SARS-CoV-2 variants, suggesting that changes in these mutated ORFs, namely ORF3a, 6, 7a and 8, have provided a selective advantage. Our understanding of the functions of ORFs in SARS-CoV-2 has been accelerated by the previous research on SARS-CoV [108]. ORF3a is a putative viral ion channel [109] implicated in autophagy inhibition [110-112], inflammasome activation [113, 114], and apoptosis [115]. ORF6 has been shown to block type I interferon production and signaling by preventing nuclear translocation of IRF3 and STAT1 [19, 20]. SARS-CoV-2 ORF7a, similar to its homolog in SARS-CoV, has been demonstrated to inhibit the antiviral restriction factor tetherin [116, 117]. ORF9b is upregulated at the RNA and protein level in the alpha variant, which results in enhanced replication through the reduction or delay of early host innate immune responses [6]. A similar manipulation of innate immune responses has also been proposed for the delta, gamma, and omicron variants, albeit by different mechanisms. In these variants, nucleotide substitutions at genome positions 28881-28883 can alter the production of sub-genomic N RNA [6], thereby reducing innate immune recognition [118]. Finally, SARS-CoV-2's accessory protein ORF8 is the more enigmatic, as it only shares a 20% protein identity with SARS-CoV. For SARS-CoV-2, ORF8 is a secreted glycoprotein, and diverse immunomodulatory functions have been proposed, such as IL-17A mimicry [119] and downregulation of MHC class I [7], although the full spectrum of ORF8's functions and mechanisms of action remain to be elucidated. In our model, deletion of ORF8 resulted in a change of tropism, away from the URT and towards the lower respiratory tract. We argue that this switch led to a slightly reduced transmission efficiency. We further argue that this is not due to an overall attenuation of SARS-CoV-2 lacking ORF6 and ORF8, as these viruses replicate efficiently in the lungs of both neonatal and adult K18-hACE2 mice (Fig 4 and [60, 86]). Additional studies are needed to elucidate the role and mechanism of

individual cytokines and viral accessory proteins, such as ORF8, in SARS-CoV-2 transmission. Our neonatal mouse model of SARS-CoV-2 transmission paves the way to such future mechanistic studies, as it enables the modulation of the host's immune responses, through genetic deletion of individual pathway components for example.

Amenability to genetic manipulation sets our system apart from other animal systems for transmission studies. Mice lacking Interferon alpha and beta receptor 1 (*Ifnar1*) on the K18-hACE2 background are commercially available and would help assess the contribution of type I IFN to SARS-CoV2 transmission. Our model also allows more powered studies, as the number of contact neonatal mice is not as limited as in other animal models. More importantly, the availability of mouse-specific reagents and tools increases the potential to study virus-induced immune pathways in the host, as well as respiratory mechanics that could impact transmission, such as respiratory system resistance/elastance and inspiratory capacity. An additional advantage of our model is the inoculation procedure without anesthesia, which initiates infection in the URT before progressing to the lower respiratory tract. We argue that this route of infection may recapitulate SARS-CoV-2's natural infection route better than models using deep anesthesia, in which deep inhalation favors lower respiratory tract infection. Although inoculation with anesthesia has been shown to produce the typical lung pathology associated with COVID-19 in K18-hACE2 mice [82], this approach could have a significant impact on transmission as it circumvents the initial URT infection. Another hallmark of our model is the ability to track the progression of the index and contact infection longitudinally, due to non-invasive sampling. This provides more granularity and insight into the kinetics of viral shedding and URT viral load at the level of individuals, which illuminates our understanding of transmission efficiency.

Although these features establish our model as a unique and workable tool for studying SARS-CoV-2 transmission, other animal models, such as hamsters and ferrets, have certain

advantages over the limitations of our system. For instance, our transmission model is based on a mixture of droplet and contact transmission [70]; therefore, any variant-intrinsic differences that can be affected by airborne droplet formation and virion stability cannot be studied in our system, as opposed to the hamster model [49, 120]. An additional limitation of our model is the non-physiological expression of hACE2. The expression of the hACE2 transgene is driven by a non-native K18 promoter, allowing the infection of multiple organs and resulting in tissue expression levels that are distinct from endogenously expressed ACE2 [72, 82]. Although the expression is non-physiological, we deliberately chose K18-hACE2 mice for this first study of SARS-CoV-2 transmission in mice, since our goal was to investigate and compare transmission of early and current pandemic isolates, some of which are unable to engage murine Ace2. We recognize that extrapolating tropism changes in our model to tropism in humans warrants caution, especially if these changes are solely brought upon by changes in variant spike-ACE2 binding, i.e. through mutations in spike's receptor binding site. However, we argue that tropism changes brought upon by differences in spike processing and/or by differences in host-virus interplay can be readily interpreted using our model, since protease expression and inflammation or antagonism are unadulterated by the hACE2 transgene. Taken together, our study demonstrates how the selection amongst available animal models should be based on research scope and context, as each of them can provide valuable and non-redundant information regarding SARS-CoV-2 biology.

In summary, we established a SARS-CoV-2 transmission model using neonatal K18-hACE2 transgenic mice that characterizes the net effect of variant-inherent mutations on viral tropism and transmission and uncovers for the first time the contribution of accessory proteins to transmission. Using this tractable animal model to define the molecular mechanisms underlying SARS-CoV-2 transmission could guide the development of superior antiviral therapies and

contribute to a greater understanding of not only SARS-CoV-2, but respiratory viruses in general.

Materials and Methods

Cell lines

Vero E6 cells were cultured in Dulbecco modified Eagle medium (DMEM) (Gibco) supplemented with 10% fetal bovine serum (FBS) (Atlanta Biologicals), 1% Penn/Strep (Gibco) and 1% Amphotericin B (Gibco) at 37°C with 5% CO2.

Vero E6-TMPRSS2-T2A-ACE2 cells were cultured in DMEM (Corning) containing 4 mM L-glutamine, 4500 mg per L glucose, 1 mM sodium pyruvate and 1500 mg per L sodium bicarbonate, supplemented with 10% fetal bovine serum and 10 µg per mL puromycin (Sigma) at 37°C with 5% CO_2. All cell lines were confirmed to be mycoplasma free.

Mice

C57BL/6J and K18-hACE2 C57BL/6J (strain 2B6.Cg-Tg(K18-ACE2)2Prlmn/J) mice (Jackson Laboratories, ME) were maintained and bred in a conventional animal facility. In order to produce neonatal heterozygous K18-hACE2 C57BL/6J mice for the transmission experiments, C57BL/6J females were bred with homozygous K18-hACE2 C57BL/6J males. Pups were housed with their mother for the duration of all experiments. Animal experiments were performed in the Animal Biosafety Level 3 (ABSL3) facility of NYU Grossman School of Medicine (New York, NY), in accordance with its Biosafety Manual and Standard Operating Procedures, and following Institutional Animal Care and Use Committee (IACUC) guidelines.

Generation of Virus Stocks

All SARS-CoV-2 stock preparations and subsequent infection assays were performed in the NYU ABSL3 facility, with approval of the Institutional Biosafety Committee (IBC). The following reagents were obtained through BEI Resources, NIAID, NIH: SARS-Related Coronavirus 2, Isolate USA-WA1/2020, NR-52281, deposited by the Centers for Disease Control and Prevention; SARS-Related Coronavirus 2, Isolate hCoV-19/England/204820464/2020, B.1.1.7, NR-54000, contributed by Bassam Hallis; SARS-Related Coronavirus 2, Isolate hCoV-19/South Africa/KRISP-K005325/2020, B.1.351, NR-54009, contributed by Alex Sigal and Tulio de Oliveira; SARS-Related Coronavirus 2, Isolate hCoV-19/Japan/TY7-503/2021 (Brazil P.1), NR-54982, contributed by National Institute of Infectious Diseases. SARS-CoV-2 Delta variant (hCoV19/USA/PHC658/2021) and SARS-CoV-2 Omicron BA.1 (hCoV-19/USA/GA-EHC-2811C/2021) were kindly provided by the Suthar Lab at Emory University. The USA-WA1/2020 stock was produced as previously described [121]. The other SARS-CoV-2 viruses were passaged once in Vero E6 cells supplemented with 1 µg/ml of l-1-tosylamido-2-phenylethyl chloromethyl ketone (TPCK)-trypsin, to avoid virus adaptation to Vero E6 cells due to the lack of TMPRSS2 expression. Cells were infected at an MOI of 0.01 and harvested at 50% cytopathic effect (CPE). After harvest, virus was purified using a 25% sucrose cushion at 25,000 RPM for 3-4 hours and resuspended using PBS prior to infection. For the B.1.1.7, B.1.1.351 and P.1, stocks, aliquots were initially plaque-purified and sequenced to verify the variant signature before expanding in the presence of TPCK-trypsin to generate a passage 1 working stock. WA-1 ΔORF6, WA-1ΔORF8 and its WA-1 control were kindly provided by the Frieman Lab at University of Maryland School of Medicine [86]; aliquots were used as provided for the experiments. For heat-inactivated (HI) SARS-CoV-2 WA-1, viral stocks were incubated at 56ºC for 5 hours. Samples were titered for confirmation of complete inactivation of infectious particles.

Immunohistochemistry on mouse heads

Pups infected as described above were euthanized according to humane, IACUC-approved procedure at 2 dpi. The skin of heads was gently removed to preserve nasal structures. Heads were then removed and submerged in PBS at 4°C for a brief wash, followed by fixing in 4% paraformaldehyde for 72 h at 4°C without shaking. Heads were then washed in PBS at 4°C with gentle swirling for 20 min, followed by decalcification into 0.12M EDTA solution at 4°C with gentle shaking for 7 days. Intact heads were then processed through graded ethanols to xylene and infiltrated with paraffin in a Leica Peloris automated tissue processor. Paraffin-embedded sections were stained with SARS-CoV-2 N protein antibody at a 1:300 dilution and DAPI. Slides were scanned on an Akoya Polaris Vectra imaging system. Images were viewed and prepared with Omero software prior to exporting as TIF files.

Virus infection, shedding, and transmission.

Index pups in a litter (4 to 7 days of age) were infected with a 3 µL sterile PBS inoculum without general anesthesia (to avoid direct lung inoculation) by intranasal instillation of 30 PFU of SARS-CoV-2 WA-1, SARS-CoV-2 variant or recombinant SARS-CoV-2 and returned to the litter for the duration of the experiment. Shedding of virus was collected by dipping the nares of each mouse into viral medium (PBS plus 0.3% bovine serum albumin [BSA]) daily, and samples were evaluated via quantitative reverse transcription-PCR (RT-qPCR) or plaque assay. Intra-litter transmission was assessed by collecting shedding samples daily in the littermates (contact). The pups and mother were euthanized by CO_2 asphyxiation followed by cardiac puncture. The upper respiratory tract (URT) was subjected to a retrotracheal lavage (flushing of 300 µL PBS from the trachea and collecting through the nares), and samples were used to quantify virus (via plaque assay or qRT-PCR). Ratios of index to contact pups ranged from 1:6-9 for variant comparison to 1:3-1:4 for model optimization with WA-1.

Viral quantification RT-qPCR

RNA extractions were performed using the Qiagen QIAamp Viral RNA kit. The number of viral N copy number per uL was quantified by RT-qPCR using the Taqman® RNA-to-CT One-Step RT-PCR kit (Applied Biosystems™) with SARS-CoV-2 primers and probe targeting an amplicon in the N protein of SARS-CoV-2 WA-1 (Forward: 5'ATGCTGCAATCGTGCTACAA3'; reverse: 5' GACTGCCGCCTCTGCTC3') and the probe 5'/56-FAM/TCAAGGAAC/ZEN/AACATTGCCAA/3IABkFQ/3'. A standard curve was generated for each dataset using in vitro transcribed SARS-CoV-2 N RNA sequence (MN985325.1).

Viral quantification

Infectious viral titers were determined by plaque assay. In brief, 10-fold dilutions of each virus in DMEM + 1% antibiotic/antimycotic (Gibco) were added to a monolayer of Vero E6 or Vero E6-TMPRSS2-T2A-ACE2 cells for 1 h at 37ºC. Following incubation, cells were overlaid with 0.8% agarose in DMEM containing 2% FBS and incubated at 37ºC for 36 hrs. Cells were fixed with 10% formalin, the agarose plug removed, and plaques visualized by crystal violet staining. Samples obtained from mouse experiments (shedding, lavage, and lung homogenates) were tittered in Vero E6-TMPRSS2-T2A-ACE2 to increase system sensitivity while stocks and inoculum for each transmission event were tittered in Vero E6.

Lung viral titer quantification

Lungs were collected in 500 µL of DPBS containing one stainless steel bead (QIAGEN), homogenized with the Tissue-Lyser II (QIAGEN), and debris were pulled down at 8000 rpm for 8 min. Viral titers were determined by plaque assay using Vero E6-TMPRSS2-T2A-ACE2 cells.

Cytokine and chemokine protein measurements

Cytokine and chemokine levels were measured in mouse serum using the Bio-Plex Pro Mouse Cytokine 23-plex Assay (Bio-Rad). Cytokines and chemokines were recorded on a MAGPIX

machine (Luminex) and quantitated via comparison to a standard curve. xPONENT version 4.3.229.0 software was used for the data collection and analysis. Clustered heatmaps were generated using the ComplexHeatmap package in program R v.4.1.2 [122]

Quantification and statistical analysis

All statistical analyses were performed using GraphPad Prism. Each experiment was completed at least two independent times with internal biological duplicates unless otherwise noted in the figure legends. The exact number of biological replicates (n) can be found in the figure legends. Data are represented as the geometric mean ± geometric standard deviation (SD). Kruskal-Wallis, one-way and two-way ANOVA tests with Bonferroni post hoc test, log-rank Mantel-Cox test, and *** statistical tests were performed and specifically indicated in the figure legends. P values > 0.05 were considered non-significant (ns), * $p < 0.05$, ** $p < 0.01$, *** $p < 0.001$, **** $p < 0.0001$.

Acknowledgements

We thank Thomas M. Moran, Icahn School of Medicine at Mount Sinai, and Luis Martínez-Sobrido, Texas Biomedical Institute, for the kind gift of mouse monoclonal SARS-CoV N antibody 1C7, and Mehul Suthar, Emory School of Medicine, for the gift of SARS-CoV-2 variant isolates. We are grateful to the SARS-CoV-2 Assessment of Viral Evolution Program for critical input on our data. Histopathology of human airway cultures was performed by Mark Alu, Branka Brukner Dabovic, and Cynthia Loomis from the NYUMC Experimental Pathology Research Laboratory. We are also grateful to Adriana Heguy from the NYU Genome Technology Core for deep-sequencing of all viruses used in this study.

Both the Experimental Pathology Research Laboratory and the NYU Genome Technology Core are supported by NYU Cancer Center support grant P30CA016087 and by NYU Langone's Laura and Isaac Perlmutter Cancer Center. Research was further supported by grants from NIH/NIAID (R01AI143639 to M.D., K08AI141759 to MBO), funds by The Vilcek Institute of Biomedical Graduate Sciences to B.A.R., and by NYU Grossman School of Medicine Startup funds to M.D.

References

1. Callaway, E., *What Omicron's BA.4 and BA.5 variants mean for the pandemic.* Nature, 2022. **606**: p. 848-849.
2. Qu, P., et al., *Evasion of Neutralizing Antibody Response by the SARS-CoV-2 BA.2.75 Variant.* bioRxiv, 2022.
3. Kyriakidis, N.C., et al., *SARS-CoV-2 vaccines strategies: a comprehensive review of phase 3 candidates.* npj Vaccines, 2021. **6**(1): p. 28.
4. Meng, B., et al., *Altered TMPRSS2 usage by SARS-CoV-2 Omicron impacts infectivity and fusogenicity.* Nature, 2022. **603**(7902): p. 706-714.
5. Xia, H., et al., *Evasion of Type I Interferon by SARS-CoV-2.* Cell Reports, 2020. **33**(1): p. 108234.
6. Thorne, L.G., et al., *Evolution of enhanced innate immune evasion by SARS-CoV-2.* Nature, 2022. **602**(7897): p. 487-495.
7. Zhang, Y., et al., *The ORF8 protein of SARS-CoV-2 mediates immune evasion through down-regulating MHC-I.* Proceedings of the National Academy of Sciences, 2021. **118**(23): p. e2024202118.
8. Miorin, L., et al., *SARS-CoV-2 Orf6 hijacks Nup98 to block STAT nuclear import and antagonize interferon signaling.* Proc Natl Acad Sci U S A, 2020. **117**(45): p. 28344-28354.
9. Flower, T.G., et al., *Structure of SARS-CoV-2 ORF8, a rapidly evolving immune evasion protein.* Proceedings of the National Academy of Sciences, 2021. **118**(2): p. e2021785118.
10. Lubinski, B., et al., *Functional evaluation of the P681H mutation on the proteolytic activation of the SARS-CoV-2 variant B.1.1.7 (Alpha) spike.* iScience, 2022. **25**(1): p. 103589.
11. Johnson, B.A., et al., *Loss of furin cleavage site attenuates SARS-CoV-2 pathogenesis.* Nature, 2021. **591**(7849): p. 293-299.
12. Örd, M., I. Faustova, and M. Loog, *The sequence at Spike S1/S2 site enables cleavage by furin and phospho-regulation in SARS-CoV2 but not in SARS-CoV1 or MERS-CoV.* Scientific Reports, 2020. **10**(1): p. 16944.

13. Bayarri-Olmos, R., et al., *The alpha/B.1.1.7 SARS-CoV-2 variant exhibits significantly higher affinity for ACE-2 and requires lower inoculation doses to cause disease in K18-hACE2 mice.* eLife, 2021. **10**: p. e70002.
14. Li, J.-Y., et al., *The ORF6, ORF8 and nucleocapsid proteins of SARS-CoV-2 inhibit type I interferon signaling pathway.* Virus Research, 2020. **286**: p. 198074.
15. Yuen, C.-K., et al., *SARS-CoV-2 nsp13, nsp14, nsp15 and orf6 function as potent interferon antagonists.* Emerging Microbes & Infections, 2020. **9**(1): p. 1418-1428.
16. Konno, Y., et al., *SARS-CoV-2 ORF3b Is a Potent Interferon Antagonist Whose Activity Is Increased by a Naturally Occurring Elongation Variant.* Cell Rep, 2020. **32**(12): p. 108185.
17. Shemesh, M., et al., *SARS-CoV-2 suppresses IFNβ production mediated by NSP1, 5, 6, 15, ORF6 and ORF7b but does not suppress the effects of added interferon.* PLOS Pathogens, 2021. **17**(8): p. e1009800.
18. Kopecky-Bromberg, S.A., et al., *Severe acute respiratory syndrome coronavirus open reading frame (ORF) 3b, ORF 6, and nucleocapsid proteins function as interferon antagonists.* J Virol, 2007. **81**(2): p. 548-57.
19. Frieman, M., et al., *Severe Acute Respiratory Syndrome Coronavirus ORF6 Antagonizes STAT1 Function by Sequestering Nuclear Import Factors on the Rough Endoplasmic Reticulum/Golgi Membrane.* Journal of Virology, 2007. **81**(18): p. 9812-9824.
20. Schroeder, S., et al., *Interferon antagonism by SARS-CoV-2: a functional study using reverse genetics.* Lancet Microbe, 2021. **2**(5): p. e210-e218.
21. Dolgin, E., *Coronavirus variant threatens global recovery.* Nat Africa 2021.
22. Washington, N.L., et al., *Emergence and rapid transmission of SARS-CoV-2 B.1.1.7 in the United States.* Cell, 2021. **184**(10): p. 2587-2594.e7.
23. Alpert, T., et al., *Early introductions and transmission of SARS-CoV-2 variant B.1.1.7 in the United States.* Cell, 2021. **184**(10): p. 2595-2604.e13.
24. Davies, N.G., et al., *Estimated transmissibility and impact of SARS-CoV-2 lineage B.1.1.7 in England.* Science, 2021. **372**(6538): p. eabg3055.

25. Wibmer, C.K., et al., *SARS-CoV-2 501Y.V2 escapes neutralization by South African COVID-19 donor plasma.* Nature Medicine, 2021. **27**(4): p. 622-625.
26. Naveca, F., da Costa, Cristian, Nascimiento, Valdinete, Soouza, victor, Sorado, Andre, Mejia, Matilde, Pessoa, Karina, Goncalves, Luciana, Brandao Maria Julia, Jesus, michele, Pinto, Rosemary, Silva, Marineide, Mattos, Tirza, Abdalla, Ligia, Santos, Joao Hugo, Costa-Filho, Rubens, Wallau, Gabriel Luz, Mendoca Siqueira, Marilda, Delatorre, Edson, Graf, Tiago, Bello, Gonzalo, Resende, Paola Cristina. *SARS-CoV-2 reinfection by the new Variant of Concern (VOC) P.1 in Amazonas, Brazil*. 2021 [cited 2021].
27. Faria, N.R., et al., *Genomics and epidemiology of the P.1 SARS-CoV-2 lineage in Manaus, Brazil.* Science, 2021. **372**(6544): p. 815-821.
28. Duerr, R., et al., *Clinical and genomic signatures of SARS-CoV-2 Delta breakthrough infections in New York.* eBioMedicine, 2022. **82**.
29. Ong, S.W.X., et al., *Clinical and Virological Features of Severe Acute Respiratory Syndrome Coronavirus 2 (SARS-CoV-2) Variants of Concern: A Retrospective Cohort Study Comparing B.1.1.7 (Alpha), B.1.351 (Beta), and B.1.617.2 (Delta).* Clinical Infectious Diseases, 2021. **75**(1): p. e1128-e1136.
30. Reardon, S., *How the Delta variant achieves its ultrafast spread.* Nature, 2021.
31. Puhach, O., et al., *Infectious viral load in unvaccinated and vaccinated individuals infected with ancestral, Delta or Omicron SARS-CoV-2.* Nature Medicine, 2022. **28**(7): p. 1491-1500.
32. Li, B., et al., *Viral infection and transmission in a large, well-traced outbreak caused by the SARS-CoV-2 Delta variant.* Nature Communications, 2022. **13**(1): p. 460.
33. Levine-Tiefenbrun, M., et al., *Viral loads of Delta-variant SARS-CoV-2 breakthrough infections after vaccination and booster with BNT162b2.* Nature Medicine, 2021. **27**(12): p. 2108-2110.
34. Mlcochova, P., et al., *SARS-CoV-2 B.1.617.2 Delta variant replication and immune evasion.* Nature, 2021. **599**(7883): p. 114-119.
35. Eales, O., et al., *Dynamics of competing SARS-CoV-2 variants during the Omicron epidemic in England.* Nature Communications, 2022. **13**(1): p. 4375.

36. Kozlov, M., *How does Omicron spread so fast? A high viral load isn't the answer.* Nature, 2022.
37. Kozlov, M., *Omicron's feeble attack on the lungs could make it less dangerous.* Nature, 2022. **601**(177).
38. Zhang, X., et al., *SARS-CoV-2 Omicron strain exhibits potent capabilities for immune evasion and viral entrance.* Signal Transduction and Targeted Therapy, 2021. **6**(1): p. 430.
39. Hui, K.P.Y., et al., *SARS-CoV-2 Omicron variant replication in human bronchus and lung ex vivo.* Nature, 2022. **603**(7902): p. 715-720.
40. Hoffmann, M., et al., *The Omicron variant is highly resistant against antibody-mediated neutralization: Implications for control of the COVID-19 pandemic.* Cell, 2022. **185**(3): p. 447-456.e11.
41. Lu, L., et al., *Neutralization of Severe Acute Respiratory Syndrome Coronavirus 2 Omicron Variant by Sera From BNT162b2 or CoronaVac Vaccine Recipients.* Clin Infect Dis, 2022. **75**(1): p. e822-e826.
42. Planas, D., et al., *Considerable escape of SARS-CoV-2 Omicron to antibody neutralization.* Nature, 2022. **602**(7898): p. 671-675.
43. Chalkias, S., et al., *A Bivalent Omicron-Containing Booster Vaccine against Covid-19.* New England Journal of Medicine, 2022.
44. Montagutelli, X., et al., *The B1.351 and P.1 variants extend SARS-CoV-2 host range to mice.* bioRxiv, 2021: p. 2021.03.18.436013.
45. Saito, A., et al., *Enhanced fusogenicity and pathogenicity of SARS-CoV-2 Delta P681R mutation.* Nature, 2022. **602**(7896): p. 300-306.
46. Nelson, G., et al., *Molecular dynamic simulation reveals E484K mutation enhances spike RBD-ACE2 affinity and the combination of E484K, K417N and N501Y mutations (501Y.V2 variant) induces conformational change greater than N501Y mutant alone, potentially resulting in an escape mutant.* bioRxiv, 2021: p. 2021.01.13.426558.
47. Han, P., et al., *Receptor binding and complex structures of human ACE2 to spike RBD from omicron and delta SARS-CoV-2.* Cell, 2022. **185**(4): p. 630-640.e10.

48. Shuai, H., et al., *Attenuated replication and pathogenicity of SARS-CoV-2 B.1.1.529 Omicron.* Nature, 2022. **603**(7902): p. 693-699.
49. Port, J.R., et al., *Increased small particle aerosol transmission of B.1.1.7 compared with SARS-CoV-2 lineage A in vivo.* Nature Microbiology, 2022. **7**(2): p. 213-223.
50. Escalera, A., et al., *Mutations in SARS-CoV-2 variants of concern link to increased spike cleavage and virus transmission.* Cell Host Microbe, 2022. **30**(3): p. 373-387.e7.
51. Liu, Y., et al., *The N501Y spike substitution enhances SARS-CoV-2 infection and transmission.* Nature, 2022. **602**(7896): p. 294-299.
52. Abdelnabi, R., et al., *The omicron (B.1.1.529) SARS-CoV-2 variant of concern does not readily infect Syrian hamsters.* Antiviral Res, 2022. **198**: p. 105253.
53. O'Donnell, K.L., et al., *Pathogenic and transcriptomic differences of emerging SARS-CoV-2 variants in the Syrian golden hamster model.* EBioMedicine, 2021. **73**: p. 103675.
54. Yuan, S., et al., *Pathogenicity, transmissibility, and fitness of SARS-CoV-2 Omicron in Syrian hamsters.* Science, 2022. **377**(6604): p. 428-433.
55. McMahan, K., et al., *Reduced pathogenicity of the SARS-CoV-2 omicron variant in hamsters.* Med (N Y), 2022. **3**(4): p. 262-268.e4.
56. Horspool, A.M., et al., *SARS-CoV-2 B.1.1.7 and B.1.351 variants of concern induce lethal disease in K18-hACE2 transgenic mice despite convalescent plasma therapy.* bioRxiv, 2021: p. 2021.05.05.442784.
57. Zhou, B., et al., *SARS-CoV-2 spike D614G change enhances replication and transmission.* Nature, 2021. **592**(7852): p. 122-127.
58. Munster, V.J., et al., *Subtle differences in the pathogenicity of SARS-CoV-2 variants of concern B.1.1.7 and B.1.351 in rhesus macaques.* Sci Adv, 2021. **7**(43): p. eabj3627.
59. Rosenke, K., et al., *UK B.1.1.7 (Alpha) variant exhibits increased respiratory replication and shedding in nonhuman primates.* Emerging Microbes & Infections, 2021. **10**(1): p. 2173-2182.

60. Silvas, J.A., et al., *Contribution of SARS-CoV-2 Accessory Proteins to Viral Pathogenicity in K18 Human ACE2 Transgenic Mice.* J Virol, 2021. **95**(17): p. e0040221.
61. Halfmann, P.J., et al., *SARS-CoV-2 Omicron virus causes attenuated disease in mice and hamsters.* Nature, 2022. **603**(7902): p. 687-692.
62. Richard, M., et al., *SARS-CoV-2 is transmitted via contact and via the air between ferrets.* Nat Commun, 2020. **11**(1): p. 3496.
63. Kutter, J.S., et al., *SARS-CoV and SARS-CoV-2 are transmitted through the air between ferrets over more than one meter distance.* Nat Commun, 2021. **12**(1): p. 1653.
64. Kim, Y.-I., et al., *Infection and Rapid Transmission of SARS-CoV-2 in Ferrets.* Cell Host & Microbe, 2020. **27**(5): p. 704-709.e2.
65. Peacock, T.P., et al., *The furin cleavage site in the SARS-CoV-2 spike protein is required for transmission in ferrets.* Nature Microbiology, 2021. **6**(7): p. 899-909.
66. Plante, J.A., et al., *Spike mutation D614G alters SARS-CoV-2 fitness.* Nature, 2021. **592**(7852): p. 116-121.
67. Imai, M., et al., *Syrian hamsters as a small animal model for SARS-CoV-2 infection and countermeasure development.* Proceedings of the National Academy of Sciences, 2020. **117**(28): p. 16587-16595.
68. Sia, S.F., et al., *Pathogenesis and transmission of SARS-CoV-2 in golden hamsters.* Nature, 2020. **583**(7818): p. 834-838.
69. Hou, Y.J., et al., *SARS-CoV-2 D614G variant exhibits efficient replication ex vivo and transmission in vivo.* Science, 2020. **370**(6523): p. 1464-1468.
70. Ortigoza, M.B., et al., *An Infant Mouse Model of Influenza Virus Transmission Demonstrates the Role of Virus-Specific Shedding, Humoral Immunity, and Sialidase Expression by Colonizing Streptococcus pneumoniae.* mBio, 2018. **9**(6): p. e02359-18.
71. Huang, H., et al., *SARS-CoV-2 N501Y variants of concern and their potential transmission by mouse.* Cell Death & Differentiation, 2021. **28**(10): p. 2840-2842.

72. McCray, P.B., et al., *Lethal Infection of K18-hACE2 Mice Infected with Severe Acute Respiratory Syndrome Coronavirus.* Journal of Virology, 2007. **81**(2): p. 813-821.
73. Matsuyama, S., et al., *Enhanced isolation of SARS-CoV-2 by TMPRSS2-expressing cells.* Proceedings of the National Academy of Sciences, 2020. **117**(13): p. 7001-7003.
74. Hoffmann, M., et al., *SARS-CoV-2 Cell Entry Depends on ACE2 and TMPRSS2 and Is Blocked by a Clinically Proven Protease Inhibitor.* Cell, 2020. **181**(2): p. 271-280.e8.
75. Leung, N.H.L., *Transmissibility and transmission of respiratory viruses.* Nature Reviews Microbiology, 2021. **19**(8): p. 528-545.
76. Harrison, A.G., T. Lin, and P. Wang, *Mechanisms of SARS-CoV-2 Transmission and Pathogenesis.* Trends in Immunology, 2020. **41**(12): p. 1100-1115.
77. von Wintersdorff, C.J.H., et al., *Infections with the SARS-CoV-2 Delta variant exhibit fourfold increased viral loads in the upper airways compared to Alpha or non-variants of concern.* Scientific Reports, 2022. **12**(1): p. 13922.
78. Mostaghimi, D., et al., *Prevention of host-to-host transmission by SARS-CoV-2 vaccines.* Lancet Infect Dis, 2022. **22**(2): p. e52-e58.
79. Zafar, M.A., et al., *Identification of Pneumococcal Factors Affecting Pneumococcal Shedding Shows that the dlt Locus Promotes Inflammation and Transmission.* mBio, 2019. **10**(3): p. e01032-19.
80. Zangari, T., et al., *Type I Interferon Signaling Is a Common Factor Driving Streptococcus pneumoniae and Influenza A Virus Shedding and Transmission.* mBio, 2021. **12**(1): p. e03589-20.
81. Monel, B., et al., *Release of infectious virus and cytokines in nasopharyngeal swabs from individuals infected with non-alpha or alpha SARS-CoV-2 variants: an observational retrospective study.* EBioMedicine, 2021. **73**: p. 103637.
82. Winkler, E.S., et al., *SARS-CoV-2 infection of human ACE2-transgenic mice causes severe lung inflammation and impaired function.* Nature Immunology, 2020. **21**(11): p. 1327-1335.

83. Bénard, A., et al., *Interleukin-3 is a predictive marker for severity and outcome during SARS-CoV-2 infections.* Nature Communications, 2021. **12**(1): p. 1112.
84. Moriyama, M., et al., *SARS-CoV-2 variants do not evolve to promote further escape from MHC-I recognition.* bioRxiv, 2022: p. 2022.05.04.490614.
85. Harvey, W.T., et al., *SARS-CoV-2 variants, spike mutations and immune escape.* Nat Rev Microbiol, 2021. **19**(7): p. 409-424.
86. McGrath, M.E., et al., *SARS-CoV-2 Variant Spike and accessory gene mutations alter pathogenesis.* bioRxiv, 2022.
87. Lee, J.-G., et al., *Characterization of SARS-CoV-2 proteins reveals Orf6 pathogenicity, subcellular localization, host interactions and attenuation by Selinexor.* Cell & Bioscience, 2021. **11**(1): p. 58.
88. Yang, W. and J. Shaman, *Development of a model-inference system for estimating epidemiological characteristics of SARS-CoV-2 variants of concern.* Nature Communications, 2021. **12**(1): p. 5573.
89. Petrone, M.E., et al., *Combining genomic and epidemiological data to compare the transmissibility of SARS-CoV-2 variants Alpha and Iota.* Communications Biology, 2022. **5**(1): p. 439.
90. Zhang, Y., et al., *SARS-CoV-2 Rapidly Adapts in Aged BALB/c Mice and Induces Typical Pneumonia.* Journal of Virology, 2021. **95**(11): p. e02477-20.
91. Yasui, F., et al., *Infection with the SARS-CoV-2 B.1.351 variant is lethal in aged BALB/c mice.* Scientific Reports, 2022. **12**(1): p. 4150.
92. Kutter, J.S., et al., *Transmission routes of respiratory viruses among humans.* Current Opinion in Virology, 2018. **28**: p. 142-151.
93. Chan, J.F.-W., et al., *A familial cluster of pneumonia associated with the 2019 novel coronavirus indicating person-to-person transmission: a study of a family cluster.* The Lancet, 2020. **395**(10223): p. 514-523.
94. Liu, Y., et al., *Aerodynamic analysis of SARS-CoV-2 in two Wuhan hospitals.* Nature, 2020. **582**(7813): p. 557-560.
95. Liu, J., et al., *SARS-CoV-2 cell tropism and multiorgan infection.* Cell Discovery, 2021. **7**(1): p. 17.

96. Hou, Y.J., et al., *SARS-CoV-2 Reverse Genetics Reveals a Variable Infection Gradient in the Respiratory Tract.* Cell, 2020. **182**(2): p. 429-446.e14.
97. Sajuthi, S.P., et al., *Type 2 and interferon inflammation regulate SARS-CoV-2 entry factor expression in the airway epithelium.* Nature Communications, 2020. **11**(1): p. 5139.
98. Sungnak, W., et al., *SARS-CoV-2 entry factors are highly expressed in nasal epithelial cells together with innate immune genes.* Nature Medicine, 2020. **26**(5): p. 681-687.
99. Huang, N., et al., *SARS-CoV-2 infection of the oral cavity and saliva.* Nature Medicine, 2021. **27**(5): p. 892-903.
100. Lukassen, S., et al., *SARS-CoV-2 receptor ACE2 and TMPRSS2 are primarily expressed in bronchial transient secretory cells.* The EMBO Journal, 2020. **39**(10): p. e105114.
101. Jackson, C.B., et al., *Mechanisms of SARS-CoV-2 entry into cells.* Nature Reviews Molecular Cell Biology, 2022. **23**(1): p. 3-20.
102. Zahradník, J., et al., *SARS-CoV-2 RBD in vitro evolution follows contagious mutation spread, yet generates an able infection inhibitor.* bioRxiv, 2021: p. 2021.01.06.425392.
103. Zhu, Y., et al., *A genome-wide CRISPR screen identifies host factors that regulate SARS-CoV-2 entry.* Nature Communications, 2021. **12**(1): p. 961.
104. Cevik, M., et al., *SARS-CoV-2, SARS-CoV, and MERS-CoV viral load dynamics, duration of viral shedding, and infectiousness: a systematic review and meta-analysis.* The Lancet Microbe, 2021. **2**(1): p. e13-e22.
105. Gao, C., et al., *Proinflammatory cytokines are associated with prolonged viral RNA shedding in COVID-19 patients.* Clinical Immunology, 2020. **221**: p. 108611.
106. Mallapaty, S., *Where did Omicron come from? Three key theories.* Nature, 2022. **602**.
107. Hu, B., et al., *Characteristics of SARS-CoV-2 and COVID-19.* Nature Reviews Microbiology, 2021. **19**(3): p. 141-154.

108. Yount, B., et al., *Severe Acute Respiratory Syndrome Coronavirus Group-Specific Open Reading Frames Encode Nonessential Functions for Replication in Cell Cultures and Mice.* Journal of Virology, 2005. **79**(23): p. 14909-14922.
109. Kern, D.M., et al., *Cryo-EM structure of SARS-CoV-2 ORF3a in lipid nanodiscs.* Nature Structural & Molecular Biology, 2021. **28**(7): p. 573-582.
110. Qu, Y., et al., *ORF3a-Mediated Incomplete Autophagy Facilitates Severe Acute Respiratory Syndrome Coronavirus-2 Replication.* Front Cell Dev Biol, 2021. **9**: p. 716208.
111. Su, W.Q., X.J. Yu, and C.M. Zhou, *SARS-CoV-2 ORF3a Induces Incomplete Autophagy via the Unfolded Protein Response.* Viruses, 2021. **13**(12).
112. Miao, G., et al., *ORF3a of the COVID-19 virus SARS-CoV-2 blocks HOPS complex-mediated assembly of the SNARE complex required for autolysosome formation.* Dev Cell, 2021. **56**(4): p. 427-442.e5.
113. Siu, K.-L., et al., *Severe acute respiratory syndrome Coronavirus ORF3a protein activates the NLRP3 inflammasome by promoting TRAF3-dependent ubiquitination of ASC.* The FASEB Journal, 2019. **33**(8): p. 8865-8877.
114. Xu, H., et al., *SARS-CoV-2 viroporin encoded by ORF3a triggers the NLRP3 inflammatory pathway.* Virology, 2022. **568**: p. 13-22.
115. Ren, Y., et al., *The ORF3a protein of SARS-CoV-2 induces apoptosis in cells.* Cellular & Molecular Immunology, 2020. **17**(8): p. 881-883.
116. Martin-Sancho, L., et al., *Functional Landscape of SARS-CoV-2 Cellular Restriction.* bioRxiv, 2020.
117. Taylor, J.K., et al., *Severe Acute Respiratory Syndrome Coronavirus ORF7a Inhibits Bone Marrow Stromal Antigen 2 Virion Tethering through a Novel Mechanism of Glycosylation Interference.* J Virol, 2015. **89**(23): p. 11820-33.
118. Ramazzotti, D., et al., *Large-scale analysis of SARS-CoV-2 synonymous mutations reveals the adaptation to the human codon usage during the virus evolution.* Virus Evolution, 2022. **8**(1).
119. Wu, X., et al., *Viral Mimicry of Interleukin-17A by SARS-CoV-2 ORF8.* mBio, 2022. **13**(2): p. e0040222.

120. Port, J.R., et al., *Host and viral determinants of airborne transmission of SARS-CoV-2 in the Syrian hamster.* bioRxiv, 2022.
121. Vries, M.d., et al., *A Comparative Analysis of SARS-CoV-2 Antivirals Characterizes 3CL^{pro} Inhibitor PF-00835231 as a Potential New Treatment for COVID-19.* Journal of Virology, 2021. **95**(10): p. e01819-20.
122. Team, R.C., *R: A language and environment for statistical computing. R Foundation for Statistical Computing*. 2022: Vienna, Austria.

Supplemental Figures

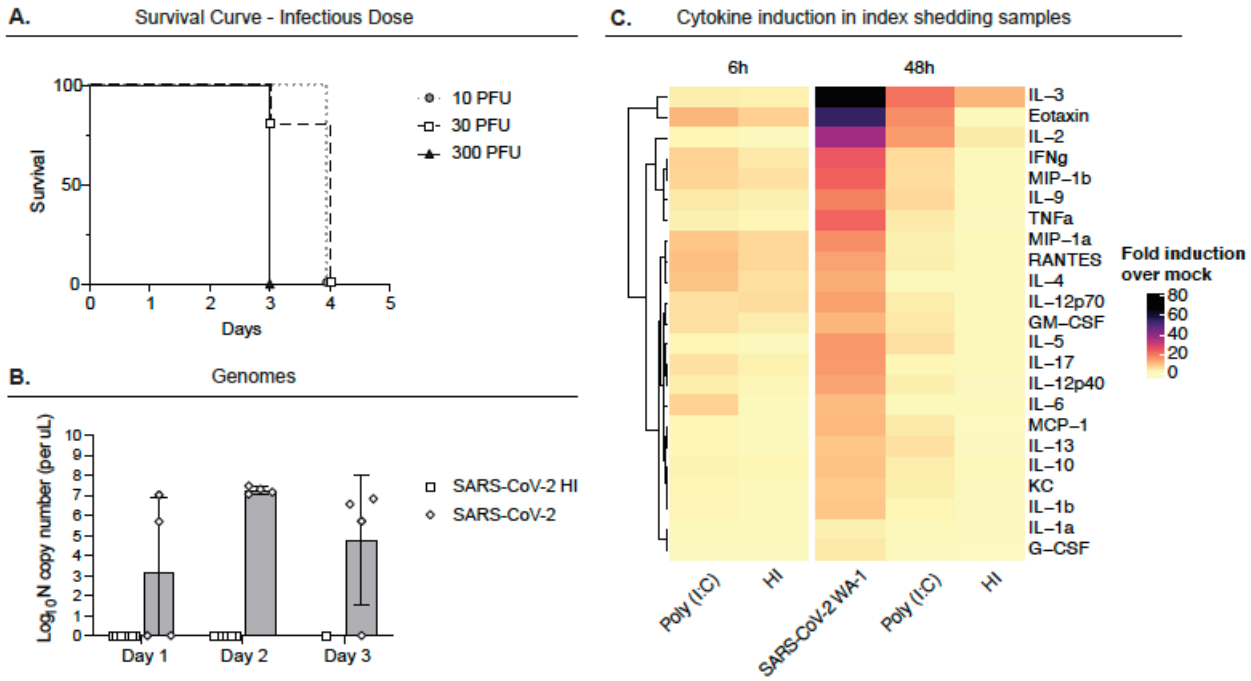

Supplemental Figure 1: Parameters establishing K18-hACE2 neonatal transmission model A) Survival curve of K18-hACE2$^{+/-}$ index pups infected with various doses of SARS-CoV-2 WA-1. At day 0 (4 to 7 days of age), index pups were infected intranasally with either 10, 30 or 300 PFU of SARS-CoV-2 WA-1 and monitored for survival daily. n = 3-5 mice/group. (B) Shedding samples from each day were evaluated individually via RT-qPCR for index mice infected with 30 PFU of SARS-CoV-2 or heat-inactivated SARS-CoV-2 (HI). Each symbol represents the shedding titer measured from a single mouse on the specified day. Bars and error bars represent geometric mean and geometric standard deviation, respectively. (C) Heatmap representing cytokine induction in the index shedding samples of mice either treated intranasally with poly (I:C) or infected with HI SARS-CoV-2 or SARS-CoV-2 WA-1 at 6 or 48 hours post-infection. Levels represent fold induction over mock-infected pups.

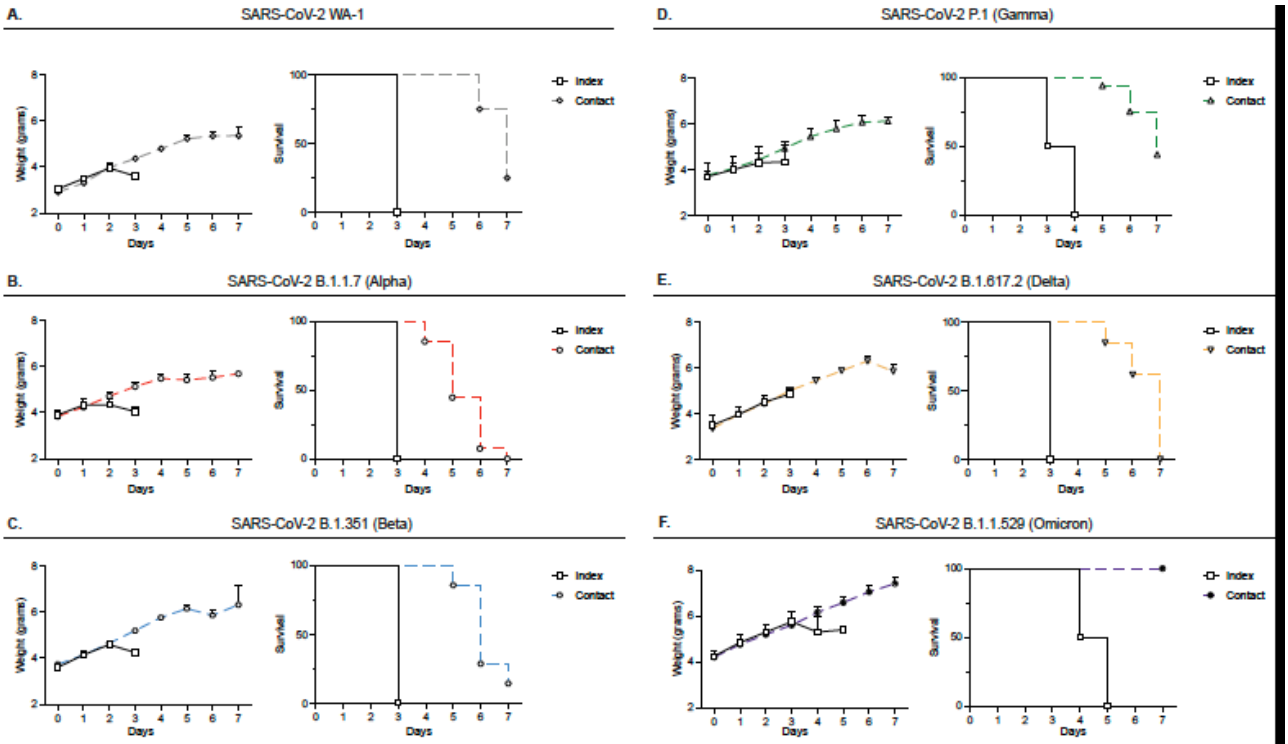

Supplemental Figure 2: Weight and survival curves of index and contact mice infected with SARS-CoV-2 variants. At day 0 (4 to 7 days of age), pups were infected i.n. with 30 PFU of SARS-CoV-2 variants (index) and cohoused with uninfected littermates (contact) for 7 days. (A-F) Left panel: Survival curve of index and contact mice after index infection with SARS-CoV-2 variants. Right panel: body weight curve of index and contact mice infected with SARS-CoV-2 variants. Data represented as mean with error bars indicating SEM. index mice n = 2-4, contact mice n = 8 - 27. (A) WA-1, (B) alpha, (C), beta, (D) gamma, (E) delta or (F) omicron.

1049
1050

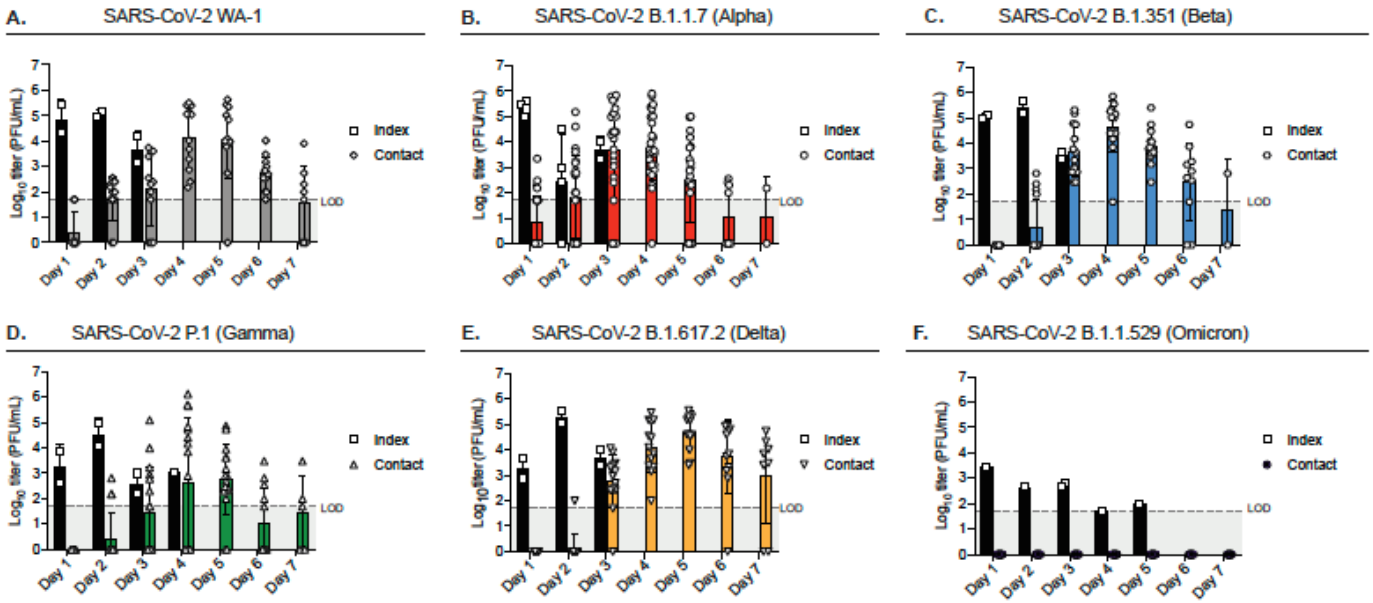

Supplemental Figure 3: SARS-CoV-2 neonatal model reveals variant transmission dynamics. At day 0 (4 to 7 days of age), pups were infected i.n. with 30 PFU of SARS-CoV-2 variants (index) and cohoused with uninfected littermates (contact) for 7 days. Ratios of index to contact was 1 index to 6-9 contacts. Shedding of SARS-CoV-2 was collected by dipping the nares of each mouse in viral medium daily. (C - G) Shedding samples from each day were evaluated individually via plaque assay for (A) WA-1, (B) alpha, (C) beta, (D) gamma, (E) delta or (F) omicron. Each symbol represents the shedding titer measured from a single mouse on the specified day. Index pups are shown by open squares and black bars, while contact mice are represented by open symbols, and colored bars. Data represents at least 2 independent repetitions. Bars denote geometric mean with geometric standard deviation. LOD: Limit of detection.

1051
1052